



technische universität
dortmund

Signal Extraction Studies applied to CTA and FACT

Master thesis

to achieve the degree of
Master of Science

presented by

B. Sc. Sabrina Einecke

born in Werne

Lehrstuhl Experimentelle Physik Vb
Fakultät Physik
Technische Universität Dortmund

2013

1. Reviewer : Prof. Dr. Dr. Wolfgang Rhode

2. Reviewer : Prof. Dr. Claus Gößling

Date of exhibition: 28. March 2013

Abstract

In the course of this thesis, signal extraction studies for different experiments within the field of gamma-ray astronomy have been accomplished. The extracted information of charge and arrival time which can be determined by various algorithms is important for the data analysis. Accordingly, various extraction algorithms have been considered, extended and adapted to the certain properties of the experiments CTA and FACT. In order to evaluate the algorithms, statistical and physical parameters have been introduced to draw comparisons and to optimize the algorithms concerning specific conditions. In this context the studies have been conducted based on simulations.

Regarding the future project CTA, the algorithms have been applied to existing low-energy simulations with different configuration parameters. For this purpose, factors to convert the integrated signal to a number of photoelectrons have been estimated. Furthermore, the algorithms have been optimized towards several adjustment parameters. Following this, the obtainable resolution for various configuration parameters has been compared and optimal integration windows depending on the distinct parameters have been determined.

The FACT project uses a new technology of photon detectors. On that account, separate simulations are necessary which have been generated subsequent to the adaption to the features of FACT. These simulations have been studied similar to the above-mentioned study.

Kurzfassung

Im Rahmen dieser Arbeit wurden Studien zur Signalextraktion für verschiedene Experimente der Gammaastronomie durchgeführt. Die extrahierten Informationen von Ladung und Ankunftszeit sind wichtig für die Datenanalyse und können mit verschiedenen Algorithmen bestimmt werden. Daher wurden einige Extraktionsalgorithmen betrachtet, erweitert und angepasst auf die speziellen Eigenschaften der Experimente CTA und FACT. Zur Bewertung der Algorithmen wurden statistische und physikalische Größen eingeführt, anhand derer zum einen Vergleiche gezogen werden können, als auch zum anderen die Algorithmen in Abhängigkeit von speziellen Gegebenheiten optimiert werden können. Die Untersuchungen fanden in diesem Zusammenhang anhand von Simulationen statt.

Bezüglich des in der Planung befindlichen Projekts CTA wurden die Algorithmen auf vorhandene niederenergetische Simulationen mit unterschiedlichen instrumentellen und physikalischen Parametern angewendet. Dazu wurden unter anderem Kalibrationsfaktoren zur Umrechnung von integriertem Signal in Anzahl an Photoelektronen abgeschätzt. Des Weiteren wurden die Algorithmen hinsichtlich einiger Einstellungsparameter optimiert. Im Anschluss wurden die erreichbare Auflösung für verschiedene Konfigurationsparameter verglichen und optimale Integrationsfenster in Abhängigkeit der unterschiedlichen Parameter bestimmt.

Das FACT Projekt arbeitet mit einer neuen Technologie von Photondetektoren. Daher war es nötig, separate Simulationen zu generieren, nachdem sie an die Gegebenheiten von FACT angepasst wurden. Diese wurden im Folgenden ähnlich der zuvor beschriebenen Untersuchung analysiert.

Contents

Contents	v
1. Introduction	1
2. Gamma-Ray Astronomy	3
2.1. Gamma-Rays	4
2.2. Sources of Gamma-Rays	5
2.3. Detection of Gamma-Rays	6
3. Imaging Air Cherenkov Telescopes	7
3.1. Extensive Air Showers and the Imaging Air Cherenkov Technique	7
3.2. MAGIC - The Major Atmospheric Gamma-ray Imaging Cherenkov Telescopes	9
3.3. CTA - The Cherenkov Telescope Array	10
3.4. FACT - The First G-APD Cherenkov Telescope	12
3.5. Photon detectors for IACTs	13
4. Signal Extraction	15
4.1. Description of the Readout Samples	16
4.2. Basic Algorithms	20
4.2.1. Charge Extraction	20
4.2.2. Arrival Time Extraction	23
4.2.3. Implementation	25
4.3. Advanced Algorithms	28
4.4. Requirements to the Algorithms	28
4.5. Evaluation Criteria	29
4.5.1. Relative Root Mean Square Error	30
4.5.2. Coefficient of Variation	30
5. Signal Extraction Study for CTA	31
5.1. Monte Carlo simulation of the readout samples	31
5.2. Calibration	32
5.3. Adjustment of the range	33
5.4. Adjustment of the ratio	34
5.5. Results and Comparisons concerning the Charge Extraction	35
5.6. Results and Comparisons concerning the Arrival Time Extraction	42

6. Signal Extraction Study for FACT	45
6.1. Monte Carlo simulation of the readout samples	45
6.2. Calibration	47
6.3. Results and Comparisons concerning the Charge Extraction	48
7. Conclusion and Outlook	53
7.1. Conclusion	53
7.2. Outlook	54
A. Appendix	55
List of Abbreviations	60
List of Figures	64
List of Tables	67
Bibliography	68
Acknowledgments	72
Selbstständigkeitserklärung	74

1. Introduction

Man must rise above the Earth

- to the top of the atmosphere and beyond -

for only thus will he fully understand the world in which he lives.

- Socrates (469 – 399 BC)

More than 2000 years later Viktor Hess rose above the Earth with a balloon and discovered hereby the cosmic rays providing a basis for a new branch in physics and astronomy. As the quotation hypothesizes, it is not satisfactory to examine just the Earth or even the Earth's atmosphere – the actual fascination is provided far beyond the atmosphere. But contrary to Socrates' statement, it is not sufficient just to rise beyond the atmosphere to fully understand the world. Questions regarding the formation of the universe, the origin of cosmic rays, the sources of high-energy particles and many more arise. In order to clarify these problems, the gamma-ray astronomy can only cover a small fraction of many interesting research fields.

Gamma-ray astronomy studies radiation from about 1 MeV – that is to say the medium-energy to ultrahigh-energy gamma-rays. These particles are particularly well suited as messenger particles from distant sources due to their electrical neutrality. For that reason, they are not deflected by intergalactic magnetic fields providing the possibility to retrace the gamma-rays to their origin. Since the number of particles decreases with increasing energy, the observation by satellites is limited by the detector volume resulting in a long measurement duration in case of ultrahigh-energy gamma-rays. Instead, the atmosphere is used as detector in an indirect method: High-energy gamma-rays interact with molecules of the atmosphere producing extensive air showers with many charged relativistic secondary particles. These particles constitute Cherenkov radiation which can be observed by ground-based detectors such as the Imaging Air Cherenkov Telescopes (IACTs) MAGIC, CTA and FACT.

The sensitivity in different energy regimes is an important characteristic of these telescopes and it is defined as the minimum observable flux of a source with a specific energy spectrum. An improvement of the sensitivity is gained for instance by a higher density of camera pixels, a larger mirror area or an increased number of telescopes. By reason that the Cherenkov Telescope Array (CTA) is still in the planning process, one can design the array particularly with regard to the sensitivity. Hence, simulation studies concerning diverse configurations including i. a. the number of telescopes of various sizes, the position of an individual telescope within the array and the properties of the readout system are in progress. This implies occasionally an optimization problem between cost and performance in different ranges of the energy spectrum [1].

In the scope of this thesis, the performance of CTA related to the electronics, more precisely the sampling rate of the readout system, is studied in view of the low-energy regime. Due to small and short Cherenkov signals and high background uncertainties in this energy range, a high sampling rate is required which results in expensive costs. Therefore different algorithms to extract the charge and the arrival time from the readout samples are to be improved and analyzed whether they are able to adjust cheaper electronics and which resolution can be obtained.

Moreover, the use of G-APDs as photon detectors - such in case of the First G-APD Cherenkov Telescope (FACT) - becomes more and more important. On that account, the algorithms developed beforehand are also applied to readout samples of FACT and optimized to the experiment's specific features.

The approach of this thesis is structured in the following steps:

Chapter 2 gives a short introduction into the gamma-ray astronomy by describing the sources and the production of gamma-rays as well as different approaches to detect them.

Chapter 3 deals with Imaging Air Cherenkov Telescopes, their ground-based detection technique and current as well as future projects using this type of telescopes. Concerning this thesis, the experiments MAGIC, CTA and FACT are relevant. Furthermore, different photon detectors for a telescope's camera are described.

Chapter 4 introduces different algorithms to extract the charge and the arrival time from the readout samples. Not only to evaluate these algorithms but also to compare various physical and instrumental parameters of the Monte Carlo simulations, different physical and statistical criteria are presented.

Chapter 5 explains a signal extraction study for CTA. Therefore it provides a description of the used Monte Carlo simulations, shows the results of the executed algorithms and analyzes these results by applying the introduced criteria.

Chapter 6 contains an equivalent signal reconstruction study for FACT. Additionally, the generating of the simulations is explained.

Chapter 7 summarizes the results and gives an outlook.

2. Gamma-Ray Astronomy

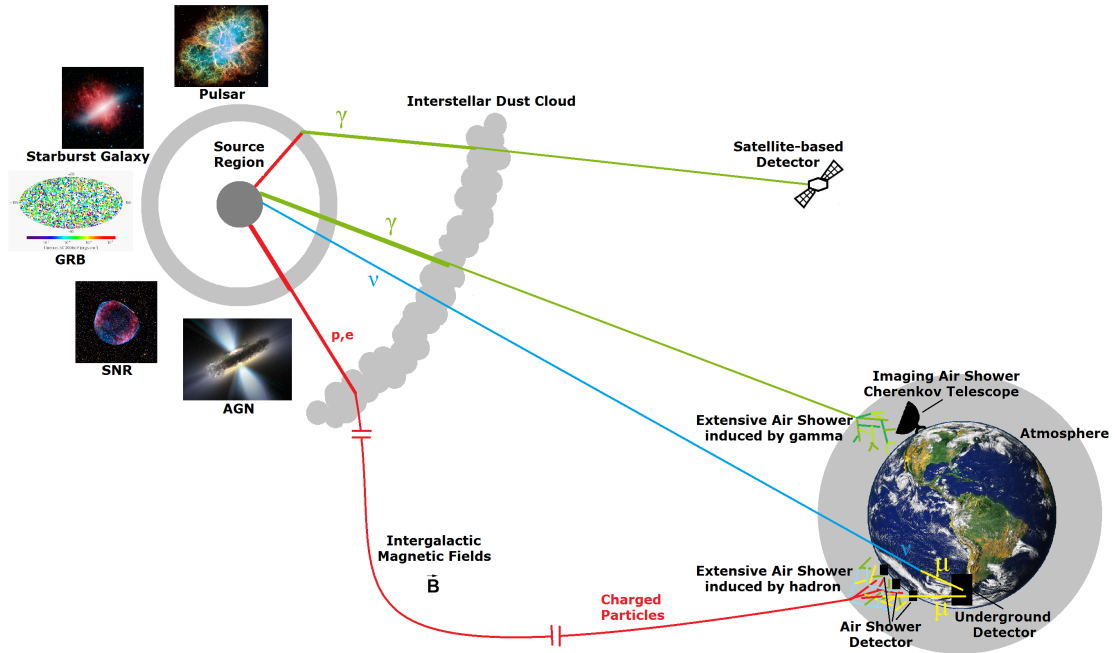


Figure 2.1.: Astroparticle physics at a schematic glance. Examples of sources emitting cosmic rays, their propagation through the universe interacting with interstellar clouds and intergalactic magnetic fields and possibilities to detect them are shown, based on [2]. The individual images stem from [3, 4, 5, 6, 7, 8].

The combination of particle physics, astronomy and cosmology turns the astroparticle physics into a most notably research field for studying the universe. In order to ascertain the processes of producing high-energy gamma radiation, the probe of celestial objects such as Active Galactic Nuclei (AGNs) or Supernova Remnants (SNRs) comprises only a small part of a wide and extremely interesting field. Figure 2 gives an overview of this field.

The radiation produced by acceleration processes within the source and its surrounding region is commonly divided in radiation of three particle types: neutrinos (ν), charged particles and photons (γ) of gamma-rays. In contrast to neutrinos and photons, charged particles are deflected by intergalactic magnetic fields and thus not traceable to their origin. That is why neutrinos and photons are most suitable as messenger particles. In order to measure the different radiation, satellite-based or ground-based detectors can be utilized.

Since this thesis covers the gamma-ray astronomy, the following sections have a focus on the processes of producing gamma-rays (section 2.1), the sources where they come from (section 2.2) and the possibilities to detect them (section 2.3).

2.1. Gamma-Rays

In the field of gamma-ray astronomy the electromagnetic fraction of the cosmic radiation is of interest, covering an energy range from about 1 MeV up to several TeV. These gamma-rays are primarily produced by non-thermal processes such as collision, annihilation, decay or acceleration.

The inelastic collision of a high-energetic cosmic ray (proton or heavier nucleus) with another one produces mainly pions (π^0 , π^+ and π^-). While charged pions decay into electrons and neutrinos, neutral pions decay instantly into two gamma-ray photons with a branching ratio of 99%:

$$\pi^0 \rightarrow \gamma\gamma \quad (2.1)$$

$$\pi^- \rightarrow \mu\nu_\mu \rightarrow e\nu_\mu\nu_e\nu_\mu . \quad (2.2)$$

In another process, an electron and its antiparticle (positron) collide and annihilate by producing gamma-rays according to

$$e^+ e^- \rightarrow \gamma\gamma \quad (2.3)$$

which is called *electron-positron annihilation*.

Moreover high-energy gamma-rays are produced by the following acceleration processes: The radiation when a charged particle is accelerated in the electric field around a nucleus is called *bremsstrahlung*.

Synchrotron radiation is emitted whenever charged particles, typically relativistic electrons, are deflected through magnetic fields which is as well an acceleration process.

Low-energy photons are upscattered by relativistic electrons (or also positrons) which transfer fractions of their energy to these photons, resulting occasionally in a gain of energy.

$$e + \gamma_{low} \rightarrow e' + \gamma_{high} \quad (2.4)$$

This mechanism is referred to as *Inverse Compton scattering*.

The question of the precise processes within a certain gamma-ray source leads in principle to two models. The leptonic model affiliates the high-energy gamma-ray production to the Inverse Compton scattering while in contrast in hadronic models it is related to the π^0 -decay. Of course also a combination of both, so-called hybrid models, is a possible scenario. For more details the reader is referred to [9].

2.2. Sources of Gamma-Rays

The sources of high-energy gamma-rays fall into two main classes, the galactic and the extragalactic sources while these classes are divided in additional subclasses. Within our galaxy, the Milky Way, supernova remnants (SNR) and pulsars are of special interest among others. Beyond our galaxy Active Galactic Nuclei (AGNs) and gamma-ray bursts (GRBs) play an important role to produce gamma-rays. These types of sources, briefly described in the following, are only a few of them, further types of high-energy gamma-ray sources are explained in [10], considering examples of certain sources.

Supernova Remnants The collapse of a star in a supernova is induced by a massive star ceasing of nuclear fusion with the result that the thermal pressure cannot resist gravity anymore. Since electrons are pushed into the core, the protons become neutrons by inverse beta decay and a degeneration pressure is created. Depending on the mass of the star, the degeneration pressure can be stopped and a neutron star or a black hole is formed. The external shell is ejected outwards forming a nebula by interactions with interstellar media. The complete object is called supernova remnant [11].

Pulsars A Pulsar is a fast rotating neutron star with a strong magnetic field emitting electromagnetic radiation along the magnetic axis. Due to the misalignment between this axis and the rotational axis, the beam is only seen periodically by an observer and the object seems to pulse. The Crab pulsar at the center of the Crab Nebula is the most famous example for a pulsar as the Nebula is commonly referred to as the *standard candle* in astrophysics [12].

Active Galactic Nuclei The term Active Galactic Nucleus [13] summarizes different extragalactic objects such as quasars, blazars, Seyfert galaxies and radio galaxies. Not only the high luminosity and time variability belong to their similarities, but in particular the radiation from compact regions at the center of the galaxy is a feature of an AGN. In contrast to that, they differ in the presence of broad emission lines, the strength of emission, the mass accretion rate, the mass of the black hole and the perspective of the observer which also determine their type. A rotating, supermassive black hole at the center of the AGN surrounded by the accretion disc is the source of power by converting gravitational potential energy. Additionally, also so-called jets can be produced along the rotational axis, emitting relativistic radiation.

Gamma-Ray Bursts Extreme luminous radiation is emitted by gamma-ray bursts which occur unforeseeable and at random positions. Since they last only from some milliseconds up to several minutes, their detection turns out to be most difficult especially for ground-based detectors because they need a certain time to re-align. Possible models of explaining gamma-ray bursts are discussed in [14].

2.3. Detection of Gamma-Rays

Since gamma-rays are absorbed by the Earth's atmosphere, it is not possible to detect them directly with ground-based instruments. In order to observe the radiation despite that, one benefits from extensive air showers induced by the interaction of gamma-rays with the atmosphere as described in section 3.1.

Particles produced within these air showers reaching ground-level can be detected by air shower arrays as for instance the Tibet Air Shower Array or water Cherenkov detectors such as the Milagro Gamma-Ray Observatory. The former Tibet Air Shower Array was able to observe gamma-rays above some TeV with multiple plastic scintillators distributed over an area of nearly $40\,000\,\text{m}^2$ [15]. The Milagro Gamma-Ray Observatory is capable to study gamma-rays above a few times $100\,\text{GeV}$ with its $60\,\text{m} \times 80\,\text{m} \times 8\,\text{m}$ (depth) pond equipped with photomultipliers and surrounded by further individual water tanks [16]. Both detector types require a background rejection of air showers initiated by hadrons which make up the largest part of all air showers. Since hadronic air showers have different features as explained in section 3.1, this is attempted by the help of muon detectors and the shower distribution on the ground. Air shower arrays allow observations of 24h a day with a field of view of about 1steradian.

In contrast to that, Imaging Air Shower Cherenkov Telescopes (IACTs) measuring the Cherenkov light produced by the particles in the air shower can only observe at night under appropriate weather conditions and with a much smaller field of view. Nevertheless they feature a much better point-source sensitivity. The Imaging Air Shower Cherenkov Technique and examples of experiments using this technique are described in the following chapter.

However, all ground-based experiments need to reconstruct the energy and the direction of the primary incident as it is only measured indirectly. An alternative straight forward approach studies gamma-rays directly with satellite-based detectors such as the Fermi Gamma-ray Space Telescope [17]. It is equipped with the Large Area Telescope (LAT), a wide-field imaging telescope and with the Gamma-ray Burst Monitor (GBM). The Large Area Telescope reconstructs the direction of the gamma-ray in a particle tracker and the energy via calorimeters, covering an energy range from below $20\,\text{MeV}$ to more than $300\,\text{GeV}$. Since the number of gamma-rays decrease with increasing energy, the observation of high-energy radiation within an acceptable measurement duration is complicated by the limited detector volume which can be installed on satellites. On that account satellites are only used to observe radiation up to some GeV.

By using the atmosphere as detector volume instead, ground-based experiments enable to study gamma-rays in an energy regime between about $30\,\text{GeV}$ and several $100\,\text{TeV}$.

3. Imaging Air Cherenkov Telescopes

Imaging Air Cherenkov Telescopes (IACTs) allow the detection of gamma-rays with ground-based instruments. This chapter will describe the Imaging Air Cherenkov Technique and it will give a short introduction to particular IACTs studied in this thesis. Furthermore photon detectors for IACTs and their characteristics are presented due to their differences concerning the signal extraction.

3.1. Extensive Air Showers and the Imaging Air Cherenkov Technique

The Earth's atmosphere protects humankind from harmful radiation of the cosmos due to its opacity in UV, X-ray or gamma-ray wavelengths. When a cosmic ray hadron or a gamma impinges on the atmosphere, it initiates extensive air showers by its interaction with nuclei of the atmosphere's molecules (N_2 , O_2 , Ar) [18]. Depending on the incident primary, different processes emerge during the shower formation as shown in Figure 3.1.

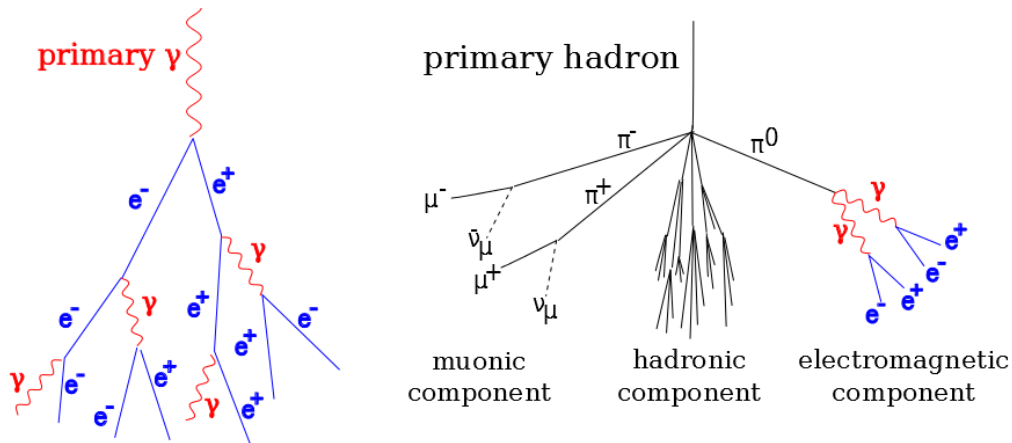


Figure 3.1.: Schematic sketch of an extensive air shower induced by a gamma-ray (left) and by a cosmic ray hadron e.g. protons or alpha particles (right).

In gamma-ray induced air showers electrons (e^-) and positrons (e^+) are created by pair production ($\gamma \rightarrow e^+ + e^-$) and photons (γ) by Bremsstrahlung where charged particles are decelerated and emit secondary photons to conserve the energy.

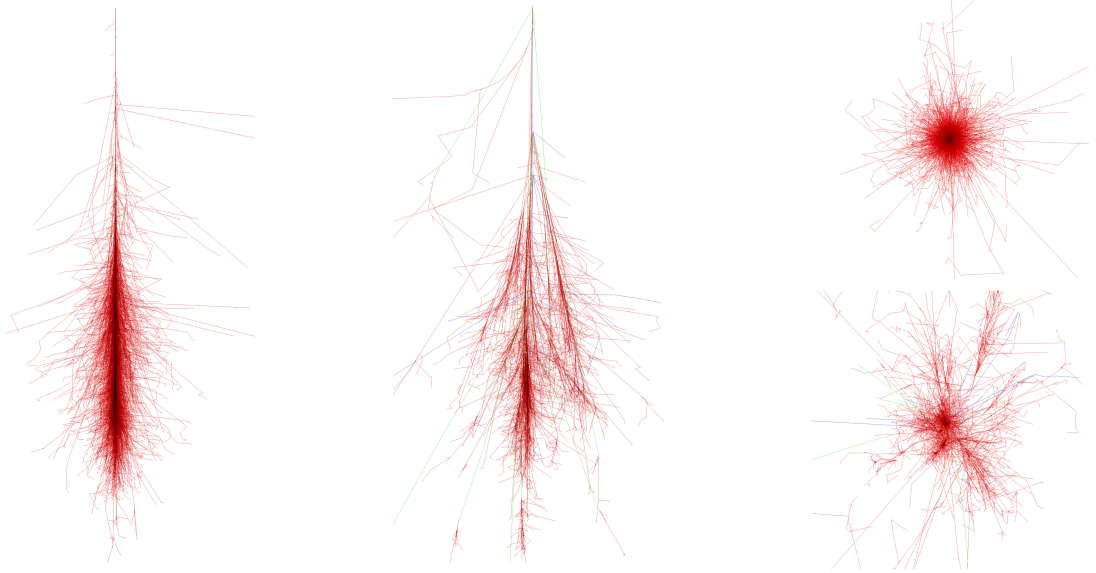


Figure 3.2.: Shower images simulated with the program CORSIKA for the longitudinal development of a shower induced by a gamma (left) and a hadron (middle) and the corresponding lateral development of a gamma-ray initiated (right top) and a hadronic (right bottom) shower. The initial energy of the incident primary is 100 GeV for both showers [20].

In contrast, air showers initiated by hadrons produce a hadronic component consisting of pions, kaons and lighter nuclei. This component propagates longitudinally along the initial momentum. The charged pions (π^+ , π^-) decay in muons and neutrinos which form the muonic component of the shower. The electromagnetic component is generated by the decay of the neutral pions (π^0) into gammas which create electrons and positrons by pair production (cp. [19]). The main processes of the shower development and the three shower components are sketched in Figure 3.1.

Large transverse momenta during the first interactions (collision and scattering) expand the lateral distribution of the shower as shown in Figure 3.2. In comparison, the gamma-ray induced shower is much more compact with a smaller lateral development.

Charged shower particles exceeding the atmosphere's speed of light emit Cherenkov radiation [21] on a narrow light cone towards the direction of the incident particle. The Cherenkov light cone from a single particle produces a ring on the ground decreasing proportional to the energy and the height above sea level. Accordingly the overlapping of several rings forms an ellipse of several hundred square meters on the ground. Due to the proportionality between the amount of Cherenkov light and the number of shower particles, the detection of this radiation allows conclusions to the energy of the incident primary.

IACTs detect Cherenkov radiation by reflecting the blueish light on a camera composed of numerous photon detectors. By the parametrization of the recorded image, the energy as well as the direction and the type of the incident particle can be determined.

3.2. MAGIC - The Major Atmospheric Gamma-ray Imaging Cherenkov Telescopes



Figure 3.3.: Picture of the MAGIC telescopes [22].

The Major Atmospheric Gamma-Ray Imaging Cherenkov Telescopes (MAGIC) belong to the biggest gamma-ray telescopes in the world and they are located at the Roque de los Muchachos on the Canarian Island La Palma, at about 2200 m above sea level. The MAGIC-I telescope started observations in 2004, since 2009 an almost identical second telescope (MAGIC-II) has been in operation. The system of two IACTs allows for stereoscopic observations in an energy regime between 50 GeV and 50 TeV (cp. [23]).

They are installed at a distance of 85 m from each other. Each telescope has a reflecting surface of around 240 m^2 and a diameter of 17 m. The individual mirrors are oriented to a hexagonal camera of about 1 m diameter composed of photomultiplier tubes (PMTs). Since 2012 MAGIC-I and MAGIC-II are equipped with identical cameras with 1039 PMTs of 0.1° . They convert the incident and from the mirror reflected rays into electronic pulses. These signals are transmitted to the control house over optical fibers (cp. [24]).

Since the upgrade in 2011 both telescopes are equipped with an ultra-fast sampling and digitizing readout system based on Domino Ring Samplers (DRS4) and external high resolution Analog-to-Digital Converters (ADCs). In this regard a sampling rate of 2 GSample/s is used (cp. [25]).

Distinctive features of the MAGIC telescopes are the fast repositioning time ($\approx 40 \text{ s}$) due to their low weight (support frame is made of carbon fibre) and the low energy threshold which enable quick follow-up observations after a gamma-ray burst (GRB) alert [26].

Some of the highlights of the MAGIC experiment were the measurement of the Crab Nebula spectrum from about 50 GeV to 50 TeV, the discovery of new very high-energy radiogalaxies and the characterization of several blazars [23].

3.3. CTA - The Cherenkov Telescope Array

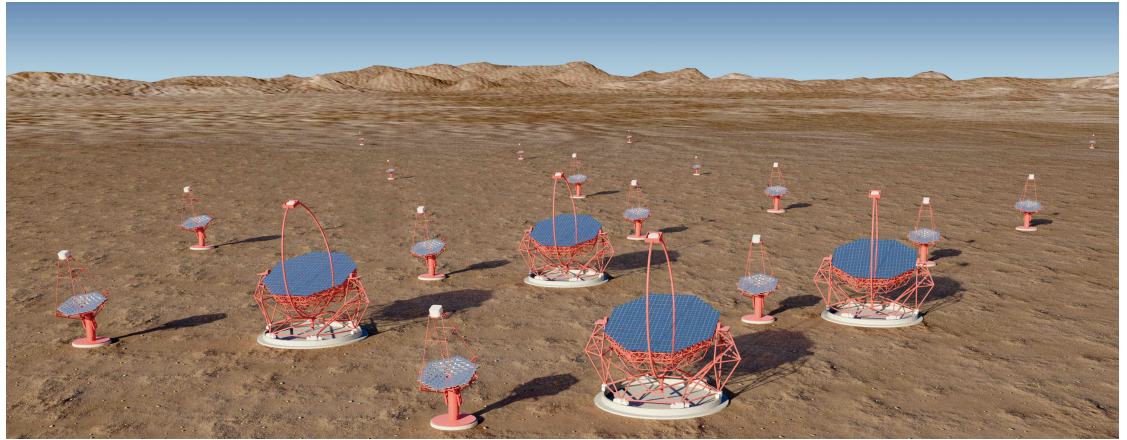


Figure 3.4.: Draft of the Cherenkov Telescope Array [27].

The Cherenkov Telescope Array (CTA) [1] is an international project to develop and construct IACTs of the next generation. It will offer a better sensitivity, an improved angular and energy resolution and an enlarged field of view compared to today's telescopes. The sensitivity in the energy regime between 100 GeV and 10 TeV will be improved by one order of magnitude. Furthermore the energy regime will be extended to lower as well as to higher energies. This allows for observations from 10 GeV to above 100 TeV.

For these purposes different sized telescopes are combined to an array of telescopes. The project will be built up of about 150 telescopes separated on a northern and a southern hemisphere array to cover the full sky. A quite appropriate design for the sites and the telescope sizes is shown in Figure 3.5. The different telescope sizes corresponding to a special energy range are described below:

Large-Size Telescopes The shower detection in the low-energy range (below 100 GeV) requires just a small array due to high event rates and background uncertainties which limit the sensitivity. On this account either many medium-size or few large-size telescopes are necessary. In case of one single medium-size telescope it is difficult to trigger the array because the signal in this energy range is small implicating too few Cherenkov photons. In contrast, combining several telescopes and their images results already for a sampling rate of 200 MSample/s in a data stream of about some TB/s.

Considering that, 3 to 4 Large-Size Telescopes (LSTs) with diameters around 24 m in a distance of about 100 m are reasonable.

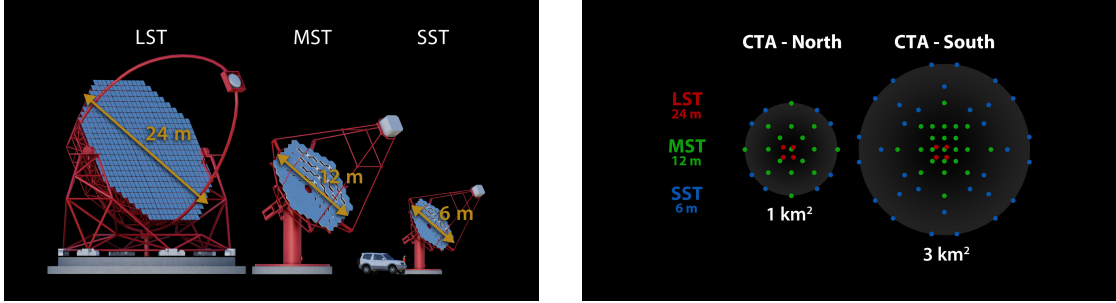


Figure 3.5.: Draft of the three telescope types (left) and possible configurations of the telescopes for the northern and the southern site [27].

Medium-Size Telescopes The Medium-Size Telescopes (MSTs) are deployed to obtain a sensitivity of one milli-Crab in the "core" energy range between 100 GeV and 10 TeV. In order to improve the sensitivity already achieved by current experiments, a larger number of telescopes to cover a huge area and improved reconstruction methods are required. The telescopes are distributed across the array which is larger than the Cherenkov light pool so that some of them are placed in an optimal distance to the shower axis. In that case a very efficient reconstruction of the energy and the direction is possible.

The MSTs will have a diameter of 10 to 15 m as well in a distance of approximately 100 m.

Small-Size Telescopes The Small-Size Telescopes (SSTs) will operate in the high-energy range above 10 TeV. Due to lower event rates in this energy regime, an area of several square kilometers is necessary to study high energetic gamma-rays.

The decision of the site is supposed to take place in the begin of 2014 and the construction of the array is estimated to start in the end of 2014. Until this particular time design concepts are studied using Monte-Carlo simulations of different configurations. Criteria to be studied are the particular number of various-sized telescopes, the position within the array, the design of the mirrors (Davies-Cotton design [28] or Schwarzschild-Couder design [29]), the properties of the electronics (e.g. the sampling rate), the technology of the photon detectors (PMTs or G-APDs, see section 3.5) and of course the costs.

CTA is intended for the pursuance of the following key projects [1]:

The origin of cosmic rays including for instance the study of galactic sources offers a large discovery potential, as well as the physics of black holes connected to the study of Active Galactic Nuclei (AGN), Extragalactic Background Light (EBL) and GRBs. Additionally, physics beyond the Standard Model are of great interest, implicating for instance the search for dark matter and the test of Lorentz invariance.

3.4. FACT - The First G-APD Cherenkov Telescope



Figure 3.6.: Picture of the FACT telescope [30].

The First G-APD Cherenkov Telescope (FACT) is a project to prove the applicability of avalanche photodiodes in Geiger-mode (G-APDs) as photon detectors in IACTs. FACT is the first IACT using this promising technology instead of photomultiplier tubes (PMTs). The advantages of G-APDs compared to PMTs are gained from the higher photon efficiency, the lower operating voltage and the insensitivity to damage due to ambient light. Accordingly, it is able to operate the telescope also during bright moonlight increasing the amount of data taking time. The telescope operates since October 2011 at the MAGIC site and recorded showers already in the first night - even during full moon [31].

For the FACT project the refurbished mount of the HEGRA CT3 telescope has been equipped with re-machined HEGRA CT1 mirrors, a new drive system and a new camera. This camera consists of 1440 Silicon Photomultipliers (SiPMs) with 3600 G-APDs each resulting in a Field of View (FoV) of 4.5° [32]. A sampling rate of 2 GSample/s is achieved by the data acquisition system with DRS-4 analogue ring sampler chips which are integrated in the camera as well as the trigger electronics [33]. The camera's and electronic's features and a total mirror area of 9.5 m^2 allow observations in an energy regime of about 300 GeV up to several TeV.

The project makes also contributions to CTA (cp. section 3.3) concerning the design of the small-sized telescopes, possible improvements of the sensitivity by the use of G-APDs and experiences of a remote operation of the telescope. Furthermore FACT is a first step towards a worldwide network of small and low-cost telescopes to enable 24/7 observations for the long-term monitoring of blazars [34]. Flare alerts given by FACT have already offered follow-up observations by other instruments.

3.5. Photon detectors for IACTs

The detection of Cherenkov radiation requires certain photon detectors to measure low intensity signals by producing and amplifying electric signals. Up to now the application of established PMTs is a common practice in the field of IACTs. However, novel G-APDs bear a huge capability and could improve the achievable sensitivity of the telescope by far. In order to prove the performance of a complete operating system with G-APDs, the FACT project described in the previous section was initiated. The general functionality of PMTs and G-APDs is briefly explained in this section. Subsequently a comparison of the advantages and disadvantages between these two types of photon detectors follows.

Photomultiplier Tubes If incident radiation strikes the photocathode of the PMT, electrons are released via the photoelectric effect. These electrons are directed towards the multiplier. By applying an electric field, the electrons are accelerated and when they strike the dynode, every electron releases a certain number of secondary electrons. This procedure of accelerating and releasing electrons is repeated with several dynodes resulting in an exponential gain of electrons. Subsequent to the last dynode, the electrons reach the anode and produce an output signal by a potential drop (cp. [35]).

A schematic of the working principle is illustrated in Figure 3.7.

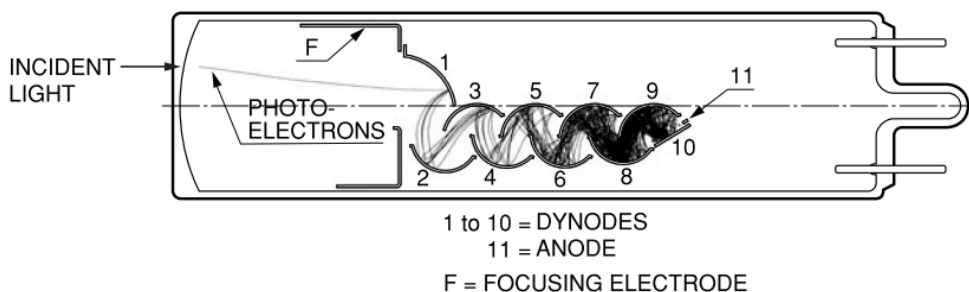


Figure 3.7.: Schematic of a photomultiplier tube [35].

Geiger-mode Avalanche Photodiodes G-APDs are semiconductors with a p-n junction operated with a reverse bias above the diode's breakdown voltage. At this junction between n- and p-type doping, a depletion layer is formed by the recombination of electrons and holes. The application of a positive voltage at the n-type part and a negative voltage at the p-type part expands this depletion region. A photon entering this region produces electron-hole pairs by the inner photoelectric effect. Due to the high electric field, these charge carriers (electrons as well as holes) induce an avalanche by collision ionization processes. A quenching circuit stops the self-sustaining avalanche in order to detect subsequent photons (cp. [36]).



Figure 3.8.: Picture of Silicon Photomultiplier (SiPM) [37].

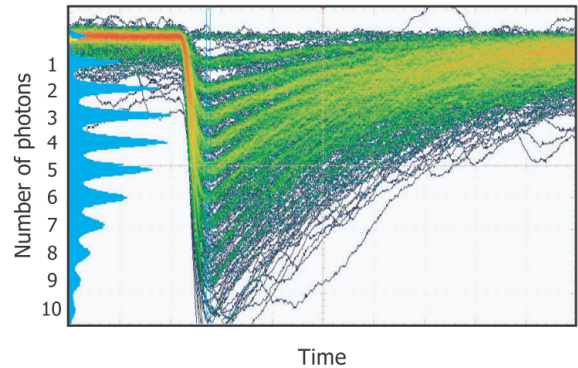


Figure 3.9.: G-APD pulse waveforms on an oscilloscope according to the number of measured photons [38].

One photodiode contains multiple cells and each of them is able to detect single photons by recognizing a breakdown. Every cell produces the same charge during its breakdown. Accordingly, the total signal as the sum of the single cells in breakdown is proportional to the number of photons and the incident radiation, respectively. Figure 3.9 shows measured pulses with different numbers of incident photons. The separation of pulses with distinct numbers can be indicated very well.

The use of novel G-APDs as photon detectors in IACTs yield several advantages compared to the established PMTs. Due to the priority objective of lowering the system's energy threshold, a main characteristic for photon detectors in IACTs is the photon detection efficiency (PDE) or the quantum efficiency (QE), respectively. Concerning PMTs the further enhancement of the QE is limited, but in case of novel G-APDs their PDE has a large potential for improvements and further developments, although their efficiency is already of the same value as the best PMTs. Moreover G-APDs versus PMTs offer the advantages of a low bias voltage (≈ 100 V instead of some kV), insensitivity to magnetic fields and no damage by bright illumination [32]. Unrequested afterpulses are produced in PMTs as well as in G-APDs, but the probability to trigger the camera is much smaller for G-APDs. This refers to the cause, that a single afterpulse occurs only in one cell of the G-APD and the resulting signal is consequently low (cp. [36]).

On the downside, the gain of the G-APDs depends strongly on the temperature which has to be compensated for instance by the use of a feedback system (as it is the case in FACT). Furthermore, an optical crosstalk may occur in G-APDs. In this instance a cell in breakdown triggers neighboring cells by emitting a photon (cp. [39]).

As the differences in the electronics and the underlying physics already suggest, the both types of photon detectors produce different pulse shapes whereby also differences concerning the signal extraction emerge. Therefore separate studies are required.

4. Signal Extraction

During the signal reconstruction the charge and the arrival time of the signal produced by Cherenkov light is to be extracted from the readout samples of the photon detectors (see section 3.5). These parameters are used in the sequel of the data analysis among other things for the calculation of the Hillas parameters [40] or for the gamma-hadron separation [41]. Using the charge of individual camera pixels which survived the image cleaning [42], for example the Hillas parameter *Size* is determined via the sum of the pixels' charge or the parameters *Length*, *Width* and *Area* by the use of the second moments of the pixels' charge. The arrival time information helps to discriminate between gammas and hadrons due to the differences in the shower duration and in the distribution of the arrival time along the shower as described in section 3.1.

The aim of current and future projects in the field of gamma-ray astronomy is to increase the sensitivity and to lower the energy threshold. For these purposes it is not enough just to increase the number of photon detectors, the number of telescopes, the mirror area or the sampling rate of the readout system. Also the analysis methods have to be enhanced. Hence, a best possible signal-to-noise ratio, a high resolution and a small bias is needed (see also section 4.5). Therefore the improvement of the charge and arrival time extraction is fundamental.

Several extraction algorithms already exist and were proposed and studied for the IACTs MAGIC (section 3.2) and VERITAS [43]. The corresponding results can be found in [44] and [45]. This thesis is geared to the above-mentioned studies, but the algorithms are extended and applied to readout samples simulated for CTA (section 3.3) and FACT (section 3.4). These simulations are described in section 5.1 and section 6.1 respectively. In comparison to the MAGIC study, they differ especially in the sampling rate of the readout system which is a distinctive factor for the performance due to its influence on the time resolution. Furthermore, the algorithms have to be adapted and optimized concerning the system's characteristics. Particularly with regard to the CTA optimization between performance and costs, this thesis deals with questions regarding the achievable sensitivity in case of specific electronic and physical parameters and whether enhanced methods are able to compensate, by way of example, slower electronics. Thus would also affect the amount of data requiring less disk space and costs.

The readout samples are described in section 4.1, moreover some notations concerning one single sample and the distribution of many samples are specified there. Section 4.2 and section 4.3 address basic algorithms for one individual pixel and advanced algorithms for all pixels. Requirements to the algorithms are described in section 4.4. In order to evaluate the performance of these extraction algorithms, section 4.5 covers the introduction of some statistical values.

4.1. Description of the Readout Samples

The photon detector's signals are transmitted to a trigger system which decides if a specific trigger condition is fulfilled. This condition might be that the signal of a particular number of pixels rise above an adjustable threshold. Subsequent to a trigger, the signals are stored by the data acquisition system. The readout samples are typically around 100 ns long to ensure that the probable Cherenkov signal is fully recorded in all pixels due to the differences in the arrival time of a Cherenkov signal.

If the electronics of the readout system sample for instance with a rate of $SR = 2\text{GSample/s}$, this will correspond to single time slices of $1/SR = 0.5\text{ns}$. In each single time slice the charge deposited during that time duration in the detector is stored. This leads to a discrete readout sample with the resolution of the readout system (cp. Figure 4.1).

In the following some useful definitions are specified:

$\langle \bullet \rangle$	Mean
S_i	Signal charge of the i -th readout sample
B_i	Background charge of the i -th readout sample
$\langle B \rangle$	Average background charge
$R_i = S_i + B_i - \langle B \rangle$	Background subtracted signal charge of i -th readout sample
S_{true}	True signal charge

(4.1)

A naive approach would just add the charge of the single time segments over a large time window. Indeed, the complete Cherenkov signal would have been collected but also a lot of night sky background (NSB) noise. The NSB can be estimated by measuring and taking the mean over a certain time. But the fact that the NSB fluctuations are not known exactly at each point in time, makes the subtraction imprecise and the resolution worse. This influences not only the image cleaning but also the calculation of the image parameters. During the image cleaning, pixels which do not belong to the shower image are removed if their charge does not exceed a certain threshold or does not fulfill specific conditions, respectively. The above-mentioned threshold has to be adapted to the NSB level. As a result of the threshold's choice and the noise fluctuations, too less or too many pixels could be removed which leads to a distorted shower image. Furthermore, also the remaining pixels contain these NSB fluctuations which falsify the calculation of the image parameters and they are notably sensitive to noise.

For all these reasons, one has to attempt to keep the error caused by noise as low as possible.

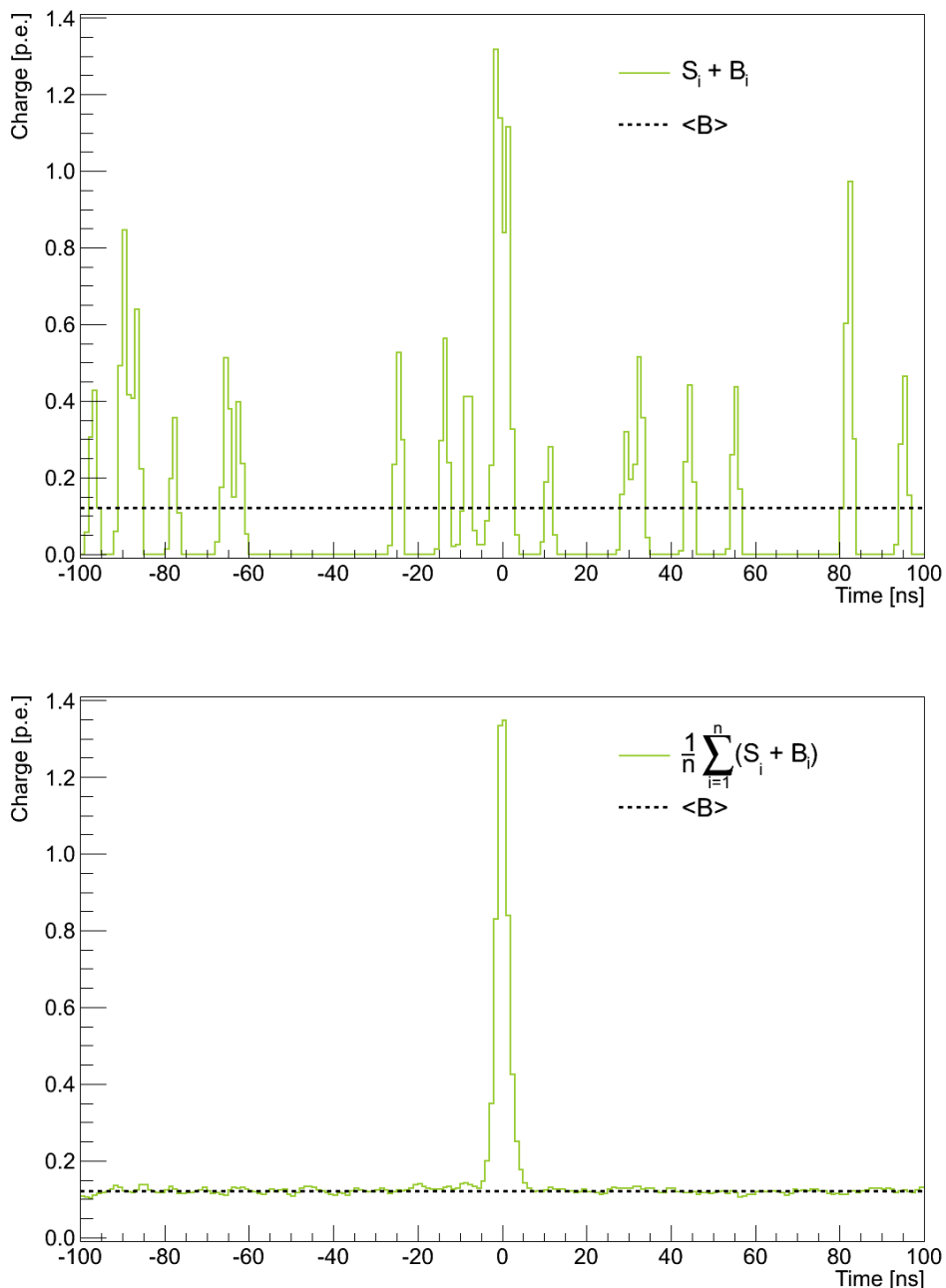


Figure 4.1.: Example of a simulated readout sample with a signal charge of 5 p.e. in the presence of night sky background (NSB) with an average rate $\langle B \rangle$ of $0.121 \frac{\text{p.e.}}{\text{ns}}$ (top) and the mean of 1000 readout samples with the same properties (bottom).

However, there exists an integration time optimizing the error of the extracted Cherenkov signal.

The outcome of a small time window is admittedly a maximal signal-to-noise ratio but noise fluctuations would effect a large impact on the signal reconstruction, especially in the low-energy regime. By using the example of a low-energy event, one single pixel measures for instance a charge of 5 photons. Is this signal contaminated by one NSB photon, an error of 20% is induced ($\frac{(5+1)\text{p.e.}}{5\text{p.e.}}$). Considering a NSB rate of $\langle B \rangle = 0.1 \frac{\text{p.e.}}{\text{ns}}$ and a window w of $w = 1\text{ns}$, the probability that this particular time slice contains the NSB photon is about 10 %. This implies again on average an error in 9 out of 10 events.

By increasing the window, the NSB content is averaged over a longer time, fluctuations are smoothed out and the noise is subtracted more precisely with a smaller error. Considering once more a NSB rate of $\langle B \rangle = 0.1 \frac{\text{p.e.}}{\text{ns}}$ and this time a window of $w = 10\text{ns}$, one NSB photon is collected on average within this window. Additionally, also the Cherenkov signal is covered in most cases within this time window. The high-energy regime requires accordingly a larger window of up to 20 ns. A window which is enlarged further would just add up additional NSB noise and the precision gets worse. Evaluation criteria to determine this time window are presented in section 4.5.

Figure 4.2 shows results obtained with different integration windows and the algorithm `ChargeSlidingSum_TimeWeightedBarycenter`, see subsection 4.2.1. The simulation of the used readout samples is described in section 5.1. The integration window of medium size (10 ns) obtains not only a distribution with the smallest deviation in respect of the true signal charge S_{true} but also the most narrow distribution which is related to a small error. A smaller window results in a comparable narrow distribution but the mean deviates more from S_{true} . In contrast, a large integration window causes a rather wide distribution even though the mean equals more or less S_{true} . The precise values of the individual distributions are listed in Table 4.1.

Window [ns]	1	10	30
Mean [p.e.]	5.49	5.01	5.03
RMS [p.e.]	1.63	1.49	2.61

Table 4.1.: Mean and RMS of the distributions corresponding to Figure 4.2.

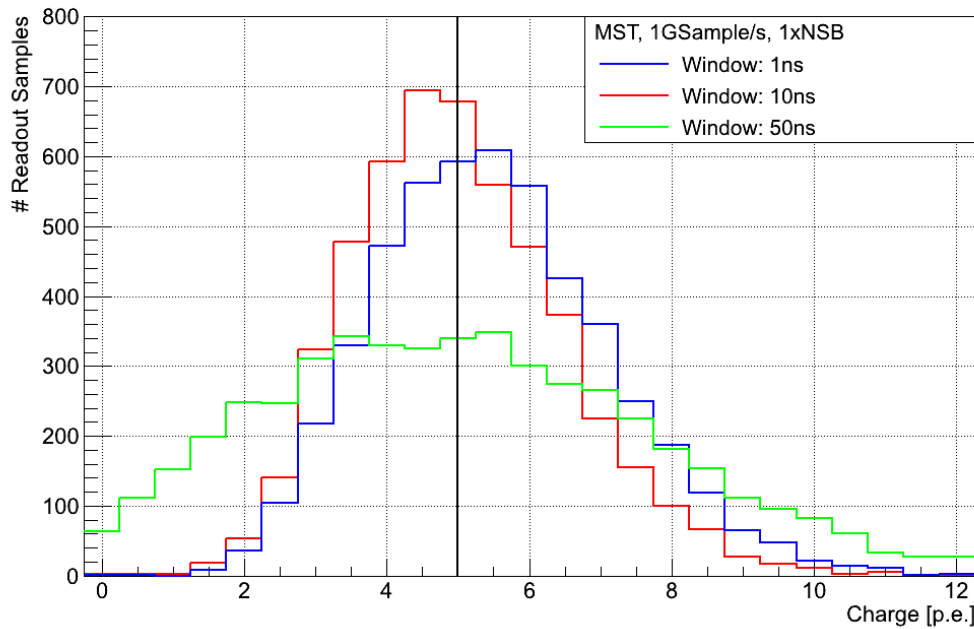


Figure 4.2.: Results of the signal charge obtained with different integration windows. The number of readout samples is plotted as a function of the signal charge. 5000 readout samples, simulated for a Cherenkov signal of 5 p.e. in a mid-size CTA telescope (MST), a NSB rate of $\langle B \rangle = 0.121 \frac{\text{p.e.}}{\text{ns}}$ and a sampling rate of $SR = 1 \text{ GSsample/s}$, are used for the evaluation. The vertical black line indicates the true signal charge S_{true} .

4.2. Basic Algorithms

In this section general methods to extract the signal charge and the arrival time from the readout sample of one individual pixel are described. Not only the combination of different charge extraction algorithms (see subsection 4.2.1) with various time extraction algorithms (see subsection 4.2.2) but also the possibility to call them with different parameters provides a lot of studies. An overview of the implementation, the classes and their functions is given in subsection 4.2.3.

4.2.1. Charge Extraction

The signal charge S or more specifically the total signal charge of the photoelectrons is proportional to the integrated signal curve. Due to the fact that the signal curve can not be described by an analytic function, numerical methods for the integration are required.

Sum The simplest method sums up the charge of the k -th time slice $S(k)$ of altogether n single time slices according to Equation 4.2. $k = 1$ to n denote all slices in a selected range.

$$S = \sum_{k=1}^n S(k) \quad (4.2)$$

Interpolation Another method performs an integration of several linear interpolations between two neighboring data points as it is shown in Figure 4.3. This equals the summation of the areas of various trapezoids. A mathematical description is represented by Equation 4.3 with the constraint that it is only valid for complete time slices. In contrast to the simple summation, it enables also the use of an arbitrary time window independent of the time slices by calculating only parts of the marginal trapezoids with the help of the interpolated function.

$$S = \left(\frac{S(1)}{2} + \sum_{k=2}^{n-1} S(k) + \frac{S(n)}{2} \right) \quad (4.3)$$

Spline As opposed to the linear interpolation also an interpolation with piecewise continuous polynomials of third degree, so-called cubic splines, can be applied. The spline interpolation leads to a smooth function with a commensurate short computing time and in comparison to a fit, an assumption of a function is not necessary. Figure 4.4 illustrates the result of a spline interpolation.

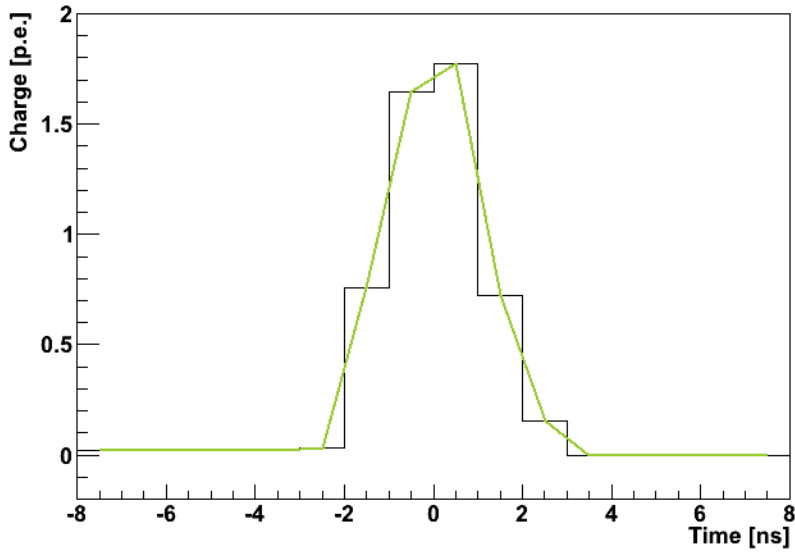


Figure 4.3.: Example of a linear interpolation. A readout sample simulated for a Cherenkov signal of 5 p.e. in a mid-size CTA telescope, a NSB rate of $\langle B \rangle = 0.121 \frac{\text{p.e.}}{\text{ns}}$ and a sampling rate of $SR = 1 \text{ GSample/s}$ is used.

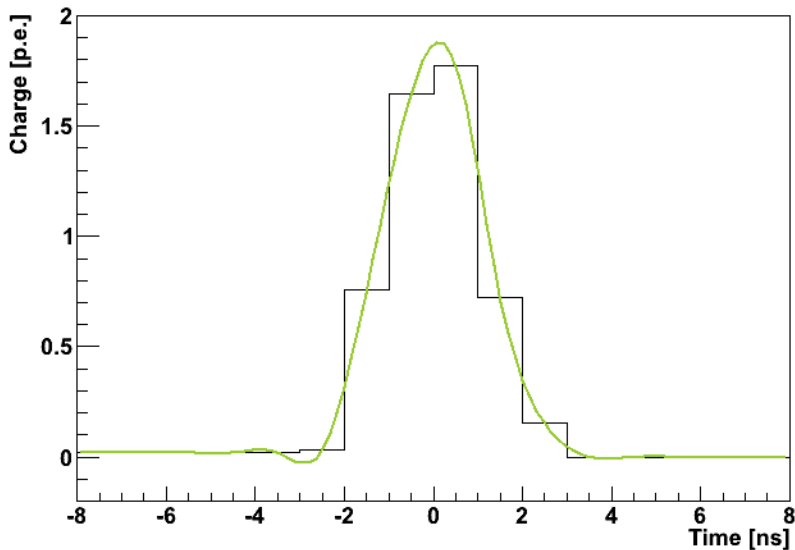


Figure 4.4.: Example of a spline interpolation. A readout sample simulated for a Cherenkov signal of 5 p.e. in a mid-size CTA telescope, a NSB rate of $\langle B \rangle = 0.121 \frac{\text{p.e.}}{\text{ns}}$ and a sampling rate of $SR = 1 \text{ GSample/s}$ is used.

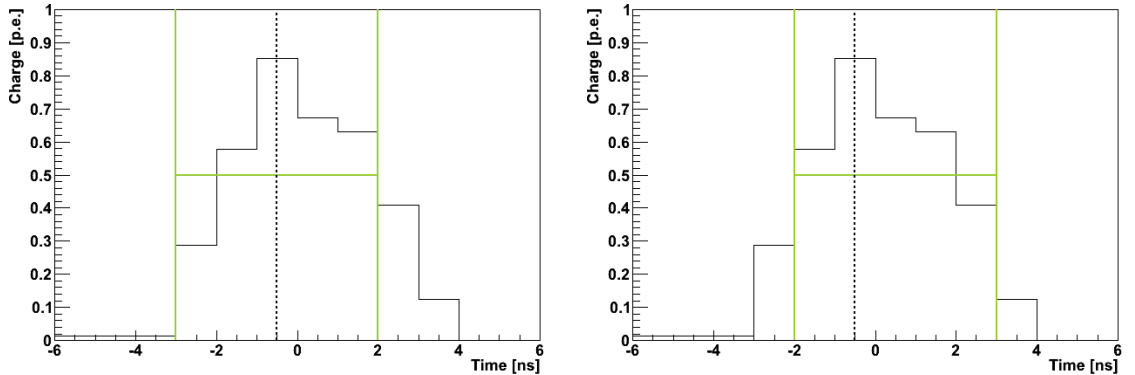


Figure 4.5.: Two examples for a fixed integration window. The position of the window is determined by the position of the maximum time slice which divides the window in a ratio of 1:1 (left) and in a ratio of 3:7 (right). A readout sample simulated for a Cherenkov signal of 5 p.e. in a mid-size CTA telescope, a NSB rate of $\langle B \rangle = 0.121 \frac{\text{p.e.}}{\text{ns}}$ and a sampling rate of $SR = 1 \text{ GSample/s}$ is used.

As described in the previous subsection, there arises the question of the width and the position of the integration window. In consequence of the NSB contaminated signal, a large integration window is not the optimal choice. Instead of that, it is preferred to keep the window relative small so that the extracted signal contains as few NSB photons as possible. This requires a well-positioned window to ensure that the bulk of the Cherenkov photons is integrated.

Fixed Window One possibility is to use an integration window of a fixed width at a certain position. This position can be determined for instance by the position of the maximum time slice which divides the window into two parts of a certain percentage. Figure 4.5 illustrates two examples for the choice of the window position.

Sliding Window In an alternative approach a sliding window of an adjustable width searches for the window position which maximizes the integrated signal. It may happen (for instance in case of a small Cherenkov signal and a large integration window) that the window which maximizes the signal, combines the Cherenkov signal with an adjacent in time NSB signal because the NSB signal is larger than the head or the tail respectively of the Cherenkov signal. This is shown in Figure 4.6.

Broadening Window A window which is broadening outwards from a maximum prevents the described cases. This algorithm starts with the maximum slice, compares the both adjacent slices and adds the larger one. This is executed until a specified width is reached. In case of small Cherenkov signals it may happen that a NSB slice is larger than the maximum slice of a Cherenkov signal. Therefore the approach is also repeated for the second to fifth maximum slice and afterwards the maximum result is chosen as the final result.

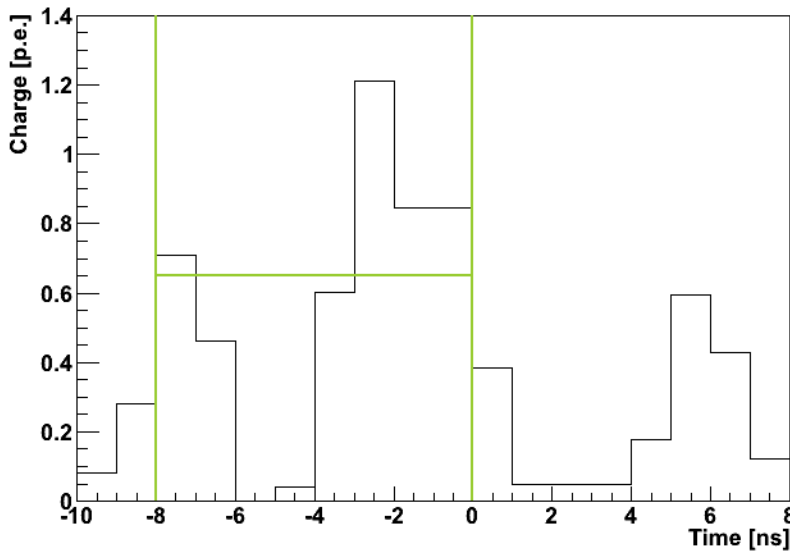


Figure 4.6.: Example of an unpreferred result of a sliding window. The signal maximizing window contains a NSB signal instead of the Cherenkov signal's tail. A readout sample simulated for a Cherenkov signal of 5 p.e. in a mid-size CTA telescope, a NSB rate of $\langle B \rangle = 0.121 \frac{\text{p.e.}}{\text{ns}}$ and a sampling rate of $SR = 1 \text{ GSample/s}$ is used.

4.2.2. Arrival Time Extraction

The arrival time t of the Cherenkov signal can be determined by different definitions which are described in the following.

Position of the maximum The position of the maximum signal in an adjustable range is one possibility to define the arrival time. If the charge is extracted by the sum or the interpolation, the arrival time will equal the center of the time slice with the maximum content. The maximum of the calculated spline will differ usually.

Position of the half maximum Another possibility specifies the arrival time as the position of the half maximum at the rising edge in a given range. This method is only possible if the charge is extracted by the interpolation or the spline due to their continuity. Supposing that the half maximum is not found in the allowed range, the left boundary will be used as arrival time.

Position of the signal-weighted barycenter An alternative approach calculates the barycenter of the time in an adjustable range, weighted with the corresponding charge $S(k)$ of the k -th time slice of altogether n single time slices according to Equation 4.4. Particularly this method depends on the choice of the position and the width of the integration time window. $k = 1, \dots, n$ denotes the selected range with arbitrary increments.

$$t = \frac{\sum_{k=1}^n S(k) \cdot k}{\sum_{k=1}^n S(k)} \quad (4.4)$$

Figure 4.7 shows an example to compare the different arrival time definitions.

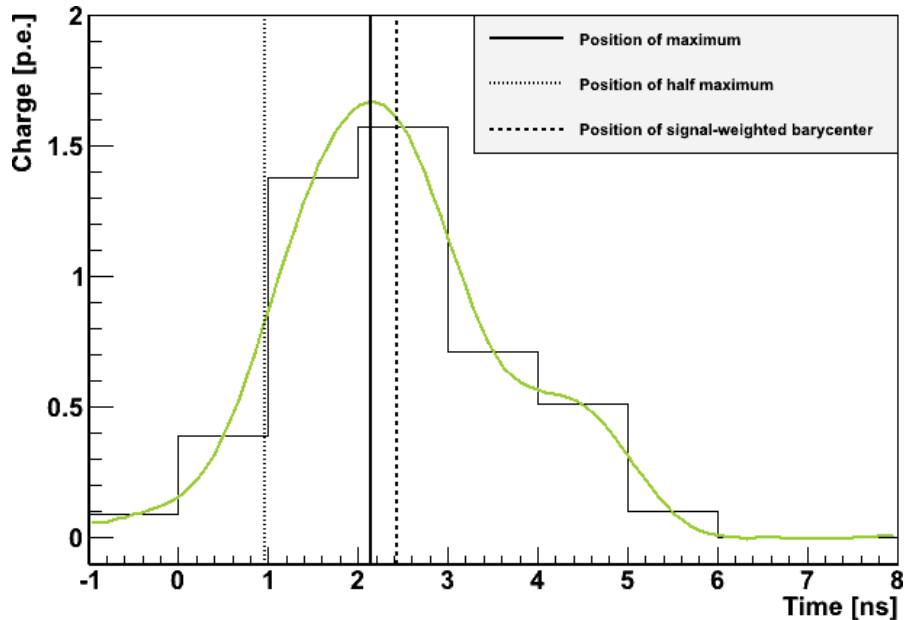


Figure 4.7.: Comparison of the different arrival time definitions by the example of a charge extraction with a spline. A readout sample simulated for a Cherenkov signal of 5 p.e. in a mid-size CTA telescope, a NSB rate of $\langle B \rangle = 0.121 \frac{\text{p.e.}}{\text{ns}}$ and a sampling rate of $SR = 1 \text{ GSample/s}$ is used.

4.2.3. Implementation

The above introduced basic methods for the integration, the determination of the window position and the definition of the arrival time are implemented in individual classes within the data analysis framework ROOT [46] which is based on C++. This allows an easy application of the classes in other more sophisticated programs. The methods are combined to the following individual classes:

ChargeFixedSum_TimeMax This class extracts the charge S by the summation of the time slices in a fixed window. The center of the time slice with the maximum content is defined as arrival time t .

ChargeFixedSum_TimeWeightedBarycenter In contrast to the previous class, the arrival time t is defined as the position of the signal-weighted barycenter of the same window used for the summation.

ChargeSlidingSum_TimeWeightedBarycenter This class differs from the previous one in the charge extraction. Instead of a fixed window a sliding window of a certain width within a range broader than the window width is applied.

ChargeFixedInterpolation_TimeHalfMax The charge S is calculated by the integration of a linear interpolation in a fixed window. Due to a fine resolution, the position of the half maximum at the rising edge determines the arrival time t in this class.

ChargeSlidingInterpolation_TimeWeightedBarycenter A sliding window in combination with the linear interpolation is called in this class to extract the charge S . As all classes which are combined with the sliding or broadening window, the position of the signal-weighted barycenter specifies the arrival time t .

ChargeBroadeningInterpolation_TimeWeightedBarycenter Compared to the previous class, the charge S is extracted in a broadening window around the maximum time slice.

ChargeFixedSpline_TimeHalfMax This class equals the ChargeFixedInterpolation_TimeHalfMax except for the application of a spline instead of a linear interpolation.

ChargeFixedSpline_TimeMax By contrast, the position of the spline maximum is taken as arrival time t in this class.

ChargeFixedSpline_TimeWeightedBarycenter Compared to the previous one, they vary only in the arrival time calculation.

ChargeSlidingSpline_TimeWeightedBarycenter Instead of a fixed window a sliding window is chosen.

ChargeBroadeningSpline_TimeWeightedBarycenter This class applies a broadening window to the integration of a spline interpolation to extract the charge S .

Within these classes several functions are implemented to receive the result, to adjust parameters or to plot miscellaneous values and pulses for the purpose of analysis and debugging. The callable functions are described below:

void SetRange (double Start, double End) By calling this function the user is able to adjust the range for the position of the integration window. The values of `Start` and `End` define the limits of the fixed window or the range where the sliding and broadening window algorithms search the window position which maximizes the signal, respectively. In case the user does not determine a range, default values for `Start` and `End` are used.

void SetWindow (double Width) The sliding and the broadening window methods need a window width which is adjusted by this function and the value of `Width`. In case the user does not set a width, a default value is used as well.

double* GetPosMaxInRange (TH1D* Pulse, double Start, double End) To determine suitable values for the function `SetRange`, it might be helpful to define them according to the position of the maximum of the histogram `Pulse` of the type `TH1D`. For instance, this position could divide a window of a certain width into two parts of a specific percentage as already shown in Figure 4.5. This function is also used for the broadening window method which additionally requires the second to fifth maximum slices. Therefore an array which contains the maximum slices is returned.

double CalcCharge (TH1D* Pulse) This function calculates the signal charge S (without background subtraction) of a pulse stored in the histogram `Pulse` of the type `TH1D`. The result is returned with double precision.

double CalcTime (TH1D* Pulse) By analogy with the function `CalcCharge`, `CalcTime` calculates the arrival time t of the pulse stored in the histogram `Pulse`.

void Draw (TH1D* Pulse) The function `Draw` plots the histogram `Pulse`.

void DrawSpline (TH1D* Pulse, int Color, int Style) As the name suggests, this function plots the spline interpolation of the histogram `Pulse` calculated within ROOT. Via `Color` and `Style` a selection of the color and the style of the plotted line is possible.

void DrawInterpolation (TH1D* Pulse, int Color, int Style) This function equals the previous one with the exception that a linear interpolation is plotted instead of a spline interpolation.

void DrawTime (int Color, int Style) The time calculated via `CalcTime` is plotted as a line in the specified color and style.

void DrawWindow (int Color, int Style) The used integration window is displayed as well in the specified color and style.

Figure 4.8 gives an overview of the implemented classes, their functions and their inheritances.

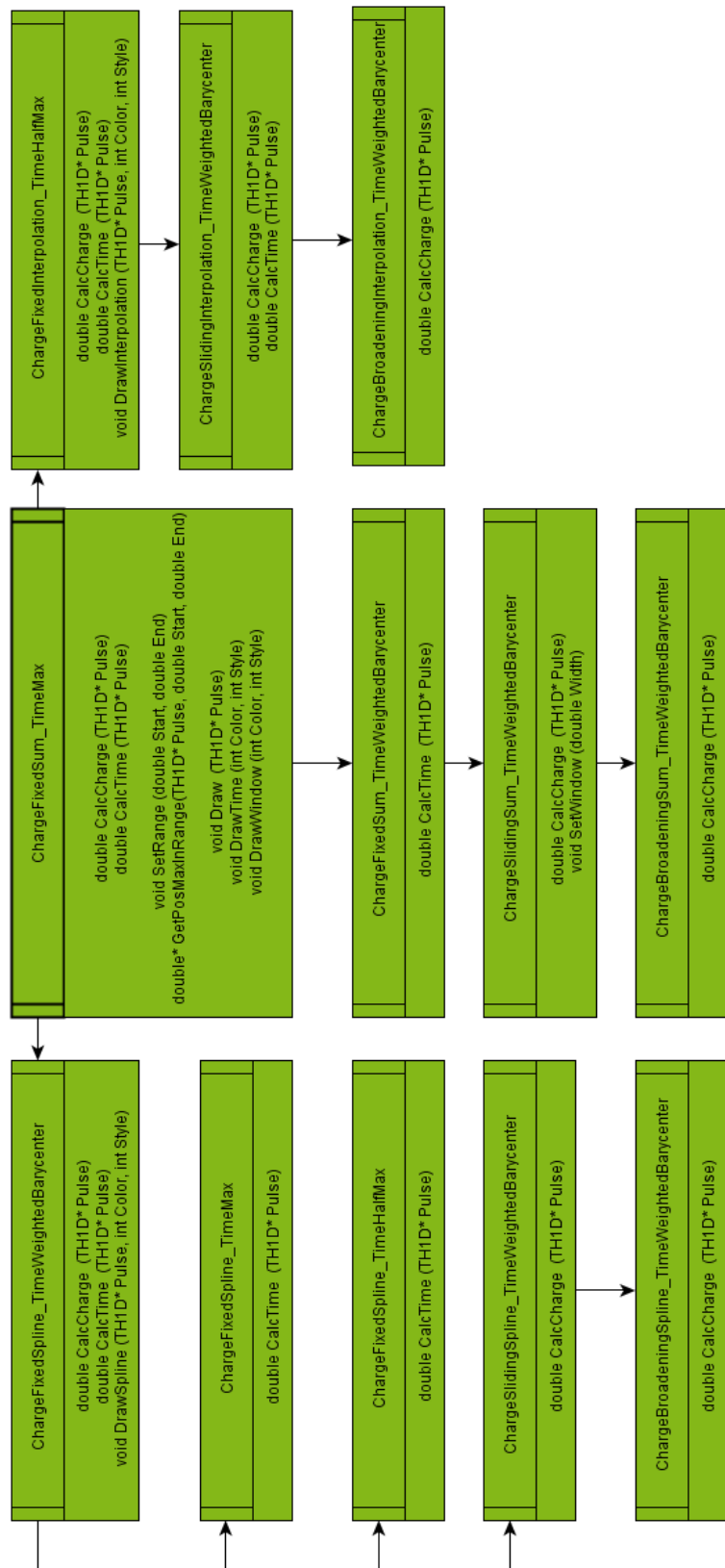


Figure 4.8.: Flow chart to illustrate the individual implemented classes, their callable functions and their inheritances.

4.3. Advanced Algorithms

In contrast to the previous section, this section introduces concepts which use the information of all pixels to determine the position of the window or at least to constrain the range where for instance the maximum signal is determined, respectively.

One opportunity is to find the pixel with the maximum charge and to use its window position also for the remaining pixels. The position of the pixel with the maximum charge is typically located at the center of the shower ellipse in the camera. Due to that, the arrival time and the corresponding Cherenkov signal position of the other shower pixels are distributed around that window position (cp. [47]).

The other idea takes also the advantage of the arrival time distribution within the shower ellipse. In a first step the arrival time is determined in a slightly broader range. Next, a linear fit of these times along the major axis of the shower ellipse is applied. The window positions are corrected by this fit and due to the optimized positioning the range can be shortened gaining an enhanced signal-to-noise ratio (cp. [45]). Additionally, this reduces the probability to extract noise instead of the Cherenkov signal and due to that the resolution of the energy and the image parameters is improved.

4.4. Requirements to the Algorithms

The introduced algorithms have to accomplish several requirements to ensure the reliability of the output and an optimal data analysis (cp. [47]).

Therefore it is important that the extracted signal charge S is proportional to the Cherenkov signal S_{true} for all signal intensities. Especially in the low-energy regime this poses a major challenge because of the same magnitude of signal and background pulses and the small pulse size which complicates for instance an efficient fit. Due to the reason that the focus of this thesis is on the signal extraction of low-energy pulses, studies of algorithms using fits were not enlarged.

In order to obtain optimal results in the further data analysis one needs an unbiased estimate of the signal charge with the highest resolution as possible. The evaluation of these criteria is of particular concern in this thesis and is described in the subsequent section.

Another requirement is the possibility to apply the algorithms in programs of different experiments and distinct features. By way of example, the properties of the electronics and in particular the sampling rate differ from experiment to experiment and this has to be taken into account by adjusting parameters of the methods.

Furthermore, the algorithms have to be robust to different background levels for instance to an increased NSB and also the computation time is relevant. Particularly with regard to the embedding of the classes in an online analysis software, the computing time has to be in the same order as the data stream.

4.5. Evaluation Criteria

As mentioned in the previous section, the algorithms have to comply certain requirements. For the evaluation a comparison between the reconstructed and the corresponding true value is drawn with the limitation that the true value is only known for simulated readout samples. Due to the presence and the fluctuation of electronic and NSB noise, samples with the same Cherenkov signal vary widely from each other. On this account, a certain amount of samples for every Cherenkov signal S_{true} is required for a statistical established evaluation.

The i -th readout sample consists of the signal charge S_i and the background B_i . Subsequent to the subtraction of the average background $\langle B \rangle$, the expression

$$R_i = S_i + B_i - \langle B \rangle . \quad (4.5)$$

is set up. Each algorithm is applied to N readout samples per configuration and per adjustment parameter. For instance the experiment, the sampling rate or the NSB level belong to the *configuration parameters*. Parameters concerning the algorithms like the range or the integration window are summarized by the term *adjustment parameters*. Consequently, a distribution of N results is obtained per parameter combination and true value. The distribution R of the single R_i is investigated in the following.

The estimate of the distribution's mean μ and the corresponding error σ_μ are calculated by these equations:

$$\mu(R) = \frac{1}{N} \sum_{i=1}^N R_i \quad (4.6)$$

$$\sigma_\mu(R) = \sqrt{\frac{1}{N(N-1)} \sum_{i=1}^N (R_i - \mu)^2} \quad (4.7)$$

An unbiased estimate of the distribution's standard deviation s (or often referred to as the RMS) and the error σ_s of this value (derived from [48]) are computed according to Equation 4.8 and Equation 4.9. Equation 4.10 defines the j -th central moment μ_j with $j = 2, 3, 4$ of R needed for Equation 4.9.

$$s(R) = \sqrt{\frac{1}{N-1} \sum_{i=1}^N (R_i - \mu)^2} \quad (4.8)$$

$$\sigma_s(R) = \sqrt{\frac{1}{N} \cdot \frac{\mu_4 - \mu_2^2 - 4\mu_1\mu_3 + 4\mu_2\mu^2}{4\mu_2}} \quad (4.9)$$

$$\mu_j = \frac{1}{N} \sum_{i=1}^N (R_i - \mu)^j \quad j = 2, 3, \dots \quad (4.10)$$

An unbiased estimate of the mean μ of the signal charge is required corresponding to a distribution distributed around the true value S_{true} . This is described by the bias b

$$b(R) = \mu(R) - S_{true} \quad (4.11)$$

which equals zero in the best case of an unbiased estimate. The standard deviation s of R is correlated with the width of the distribution R and should be as small as possible. A combination of these values $\mu(R)$ and $s(R)$ leads to statistical values (subsection 4.5.1 and subsection 4.5.2) which can be used as evaluation criteria.

Note that the described strategy to evaluate the signal charge S is equivalent to the evaluation of the arrival time t .

4.5.1. Relative Root Mean Square Error

The root mean square error (RMSE) combines the variance s^2 with the bias b (deviation between the mean μ and the true value). A small RMSE is a trade-off between a small bias and a small variance and consequently this leads to a great precision in association with a high resolution. In order to compare the RMSE of distributions with a differing signal strength S_{true} , the RMSE is normalized to a relative RMSE by dividing by S_{true} :

$$\text{rel. RMSE} = \frac{1}{S_{true}} \sqrt{s^2(R) + b^2(R)} . \quad (4.12)$$

Obviously, the evaluation of the arrival time t does not require a normalization. This value as an evaluation criterion is derived from [44].

4.5.2. Coefficient of Variation

The ratio of the standard deviation s and the mean μ defines the coefficient of variation (CV). The CV is applied to the distribution of $\ln(R)$ as proposed in [49]:

$$CV = \frac{s[\ln(R)]}{\mu[\ln(R)]} . \quad (4.13)$$

A minimal CV is correlated with maximal precision. The CV is a relative measure of dispersion independent of a measuring unit and is therefore as well suited for the comparison of different signal strengths S_{true} .

5. Signal Extraction Study for CTA

This chapter deals with the performed study of the signal extraction for CTA. It addresses particularly the issue of the signal extraction in the low-energy regime and the comparison of different configuration parameters. For these reasons, appropriate Monte Carlo simulated readout samples (hereafter referred to as MCs) are used and redescribed in section 5.1. The algorithms introduced in chapter 4 are applied to these simulated samples with various adjustment parameters. The results of the algorithm's optimization as well as their evaluation in view of the configuration parameters are presented.

5.1. Monte Carlo simulation of the readout samples

The MCs used in this CTA study were provided by S. Vorobiov (DESY Zeuthen) and generated in the context of the NECTAr (New Electronics for the Cherenkov Telescope Array) project, see [50].

Subsequent to the production of a database of several real photomultiplier pulses (sampled at 10GSample/s with a 600 MHz bandwidth oscilloscope), individual pulses of this database were scaled with the photoelectron's charge and convolved with the photonelectron's arrival time extracted from simulations of the air showers and the CTA detector. These simulations were performed with the programs CORSIKA and sim_telarray, see [51]. In order to simulate the detector, a standard configuration implicating e.g. a Davies-Cotton design, a quantum efficiency and a photoelectron spectrum of H.E.S.S. PMT Photonis XP 2960 was applied on CORSIKA showers generated within the so-called Production-1 of CTA simulations. Hereafter, the sampling rate (SR) of these pulses can be reduced, as well as the bandwidth (BW) by the application of a filter. Additionally, a contribution of the night sky background (NSB) can be added. In order to determine a NSB rate for the simulation, a dark sky at a site of good astronomical quality was assumed with a rate of $2.2 \cdot 10^{12}$ photons $\text{m}^{-2} \text{s}^{-1} \text{sr}^{-1}$. Due to different mirror dish diameters and pixel sizes of the telescope types, this corresponds to a NSB rate per pixel of 0.121 p.e./ns for the MSTs and LSTs and a rate of 0.08464 p.e./ns for the SSTs. In case of sky regions within the inner Galaxy, the NSB rate will increase by a factor of up to 4. For a more detailed description of the readout simulation the reader is referred to [49].

The MC files used in this thesis consist of 5000 readout samples each and differ from each other in the following properties: Three different charges of the Cherenkov signal (3, 5 and 8 p.e.), three different telescope types (SST, MST, LST), two different NSB rates (1 and 4 times the assumed NSB rate) and two different sampling rates and bandwidths (SRs of 250 and 1000 MSample/s, BW=SR/3.125). The file names of these MCs corresponding to a certain configuration are listed in Appendix A.

5.2. Calibration

Right at the start of the reconstruction a calibration factor to convert the integrated charge to the intended number of photoelectrons has to be determined for each algorithm and integration window. Apparently, this factor has to be constant for all number of photoelectrons. But as Figure 5.1 indicates, it is not constant for a small number of photoelectrons, especially in the case of a high NSB contribution. This is referred to the similarity between a low-energy Cherenkov signal and NSB signals with the consequence that often a NSB signal with a larger charge is extracted instead of the Cherenkov signal. The probability of such a NSB signal increases with increasing NSB contribution as a matter of course. Consequently, the signal is overestimated and the calibration factor is underestimated. The larger the Cherenkov signal, the bigger is the difference between Cherenkov and NSB signal and hence the lower is the probability for this effect. On these grounds, only readout samples with an intended number of 8 p.e. and one-times the assumed NSB rate per pixel ($1 \times \text{NSB}$) are used to estimate the calibration factor. The factor has to be determined for each algorithm, integration window and adjustment parameter separately.

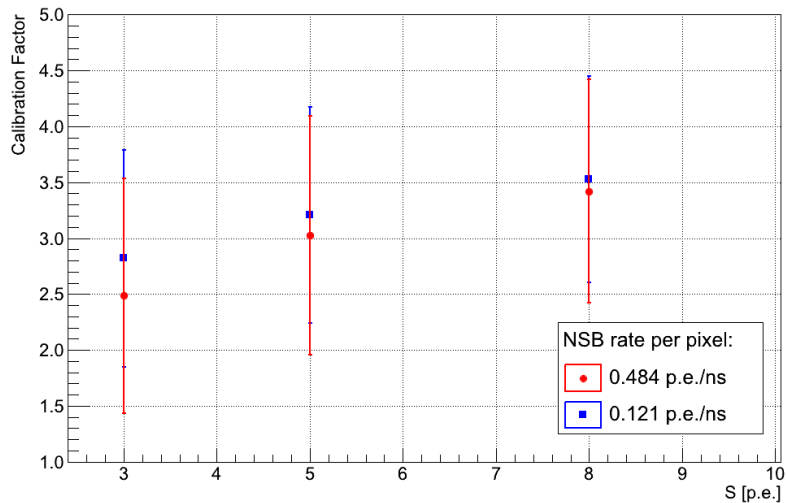


Figure 5.1.: Calibration factor as a function of the number of photoelectrons (p.e.) for different NSB rates per pixel in a mid-size CTA telescope using the example of the algorithm `ChargeFixedSum_TimeMax`. For each calculation of the factor the algorithm is applied to 5000 readout samples with a sampling rate of 1 GSsample/s. An integration window of 1 ns and a range of ± 5 ns relative to the arrival time t_0 is used.

5.3. Adjustment of the range

As described in subsection 4.2.3, the position of the integration window has to be determined. Depending on the type of the algorithm (fixed window, sliding window or broadening window), the position is determined differently and requires therefore a region of interest within the readout sample which is specified relative to a constant reference point t_0 .

For fixed window algorithms the arrival time is calculated within the preassigned region and the position of the integration window is set relative to this time. In case of a broadening window, the starting position from where the window is broadening to the defined width is sought within the preassigned range. In sliding window algorithms the preassigned region defines the range where a window of a certain width is allowed to slide.

In this section the previously mentioned range is to be adjusted and optimized. For this purpose the relative bias, RMS and RMSE as introduced in section 4.5 are considered for different combinations of the NSB rate and the number of photoelectrons. A comparison is explained in more detail in Appendix A.

The study is conducted using the example of the algorithms `ChargeFixedSpline_TimeMax`, `ChargeSlidingSpline_TimeWeightedBarycenter` and `ChargeBroadeningSpline_TimeWeightedBarycenter`. The particular algorithms are applied in each case to 5000 readout samples with a sampling rate of 1 GSample/s and an assumed NSB rate of 0.121 p.e./ns per pixel of a mid-size CTA telescope.

Considering bias, RMS and RMSE as described in Appendix A, the range is adjusted to $t_0 \pm 5\text{ ns}$ for the fixed and the broadening window algorithms since it yields advantages especially regarding to the optimization towards a small number of photoelectrons and high NSB contributions. At the same time, the selected range is large enough to ensure with a high probability that the Cherenkov signal is within this range. In contrast to the sliding window algorithms, these algorithms use the adjusted range in order to determine the arrival time which defines subsequently the position of the integration window. The range in sliding window algorithms is used to determine the position directly and therefore it has to be larger. It is adjusted to $t_0 \pm 10\text{ ns}$ so that also integration windows larger than 10 ns fit into the limited search area.

Another point of the constraint to such a small range is that in future applications the algorithms could be embedded in more advanced algorithms as described in section 4.3. These advanced algorithms provide the possibility to use a small search area by taking the information of more than one pixel into account.

5.4. Adjustment of the ratio

The fixed window algorithms require apart from the range also the declaration of a ratio. This ratio determines the position of the integration window related to the arrival time. In the following it is defined as the ratio of the left to the right range.

Since the arrival time divides the whole range into two ranges, the adjustment of the ratio has to be optimized for different arrival time determinations separately. The arrival time can be defined by the position of the maximum (`TimeMax`), the position of the half maximum at the rising edge (`TimeHalfMax`) or the position of the signal-weighted barycenter (`TimeWeightedBarycenter`).

This study is conducted using the example of `ChargeFixedSpline` algorithms applied to readout samples with a sampling rate of 1 GSample/s, a true Cherenkov signal of $S_{true} = 5$ p.e. and an assumed NSB rate of 0.121 p.e./ns per pixel of a mid-size CTA telescope. Considering the RMSE in Figure 5.2, the ratio is adjusted to 0.5 for `TimeMax`, 0.2 for `TimeHalfMax` and 0.45 for `TimeWeightedBarycenter` since these ratios yield to a good resolution while providing at the same time a short integration window. In this way, also a good signal-to-noise ratio is obtained.

The selected ratios are consistent with the characteristics of the extractors in combination with the specific pulse shape of a steep rising edge and a flat slope. Hence, the position of the signal-weighted barycenter is located more centered than the position of the maximum.

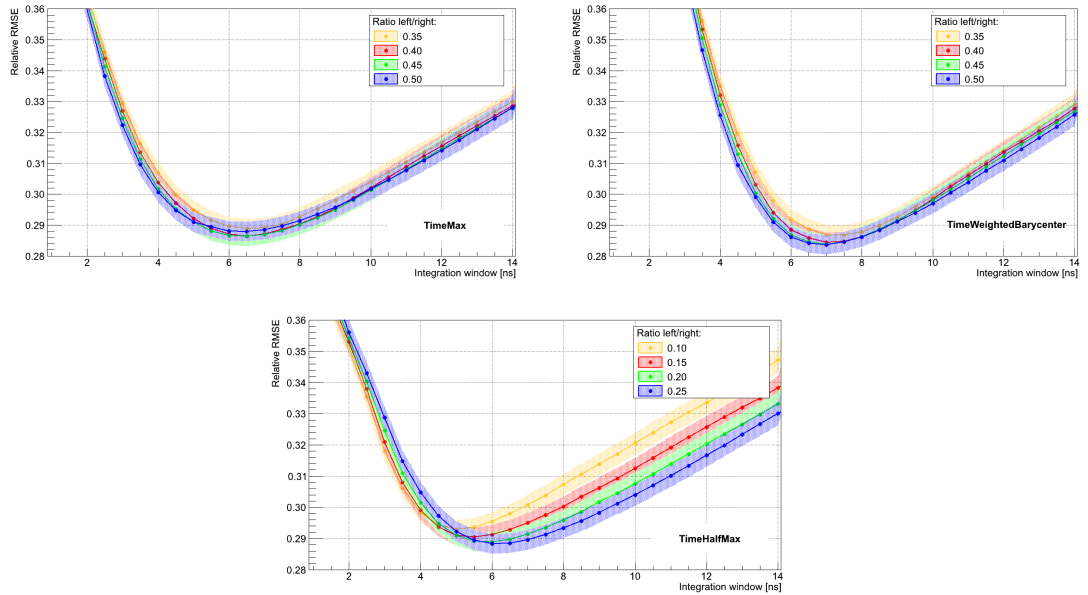


Figure 5.2.: Relative RMSE for `TimeMax` (left), `TimeWeightedBarycenter` (right) and `TimeHalfMax` (middle) algorithms as a function of the integration window. The influence of the ratio related to the arrival time using the example of `ChargeFixedSpline` algorithms is shown for 1xNSB and $S_{true} = 5$ p.e..

5.5. Results and Comparisons concerning the Charge Extraction

This section will present results obtained with different algorithms to extract the charge. For this purpose, several comparisons between the applied methods and configuration parameters as NSB rates, sampling rates and telescope sizes are drawn. It should be pointed out that not only the best resolution is of concern but also the optimal integration window. In case of similar resolutions, the algorithm with the shorter integration window should be chosen since it is related to a larger signal-to-noise ratio.

Comparison of Window Methods

Figure 5.3 and Figure 5.4 illustrate a comparison between the window methods Fixed, Sliding and Broadening of different algorithms ordered by their integration method. The method of a sliding window obtains for all integration methods the best resolution with an optimal integration window of about 6 ns (optimized for $S_{true} = 5$ p.e., samples with a different value have usually another optimal integration window). Both integration methods using the interpolation and the spline have a similar RMSE for the different window methods. In contrast, the algorithms using the sum integration method show more differences in their resolution which is referred to the cause that this method uses only discrete time slices.

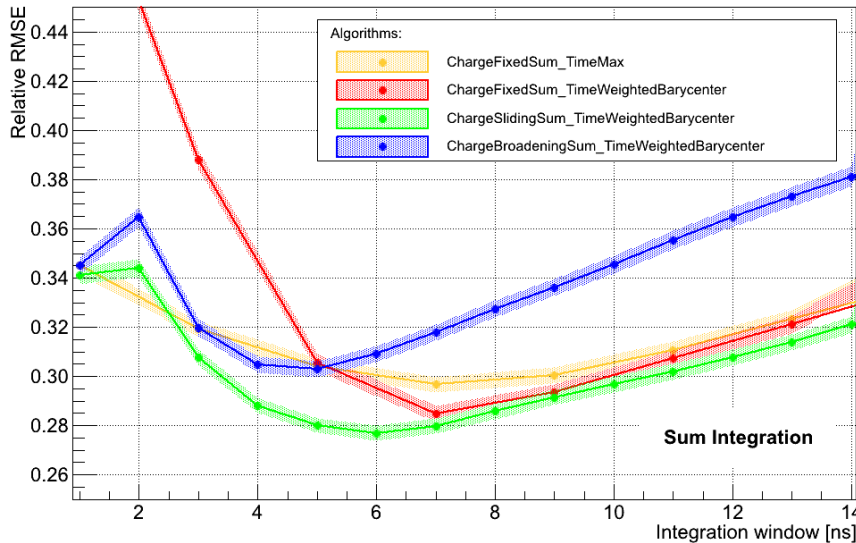


Figure 5.3.: Relative RMSE as a function of the integration window for algorithms using the integration method **Sum**. Readout samples with 1xNSB and $S_{true} = 5$ p.e. have been used.

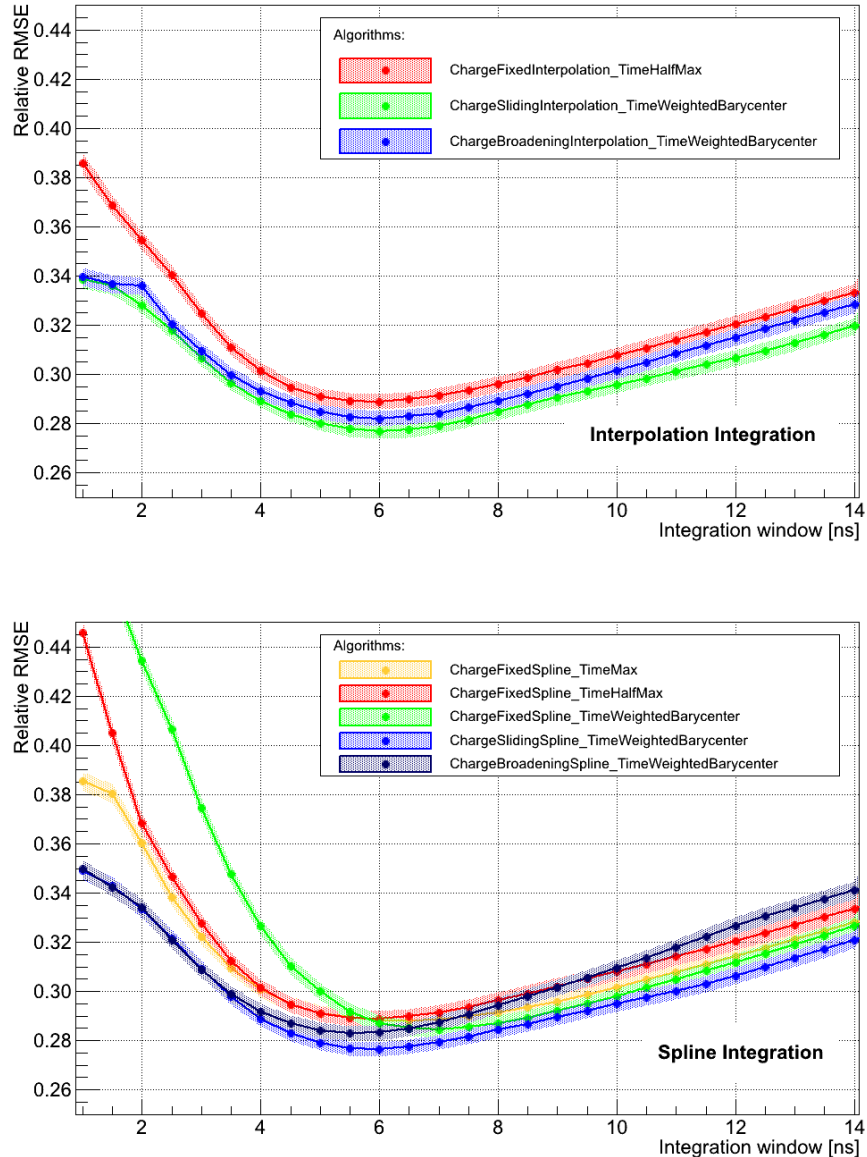


Figure 5.4.: Relative RMSE as a function of the integration window for algorithms using the integration methods **Interpolation** (top) and **Spline** (bottom). Readout samples with 1xNSB and $S_{true} = 5$ p.e. have been used.

Comparison of Integration Methods

Figure 5.5 and Figure 5.6 collate the integration methods Sum, Interpolation and Spline of different algorithms ordered by their method to position the integration window.

In general, it is ascertained that algorithms with the same window and arrival time method using an interpolation or a spline integration do not vary significantly. The survey of the fixed window algorithms presents the case that algorithms obtain similar resolutions but with a diverse optimal integration window. Indeed, the algorithm `ChargeFixedSpline_TimeWeightedBarycenter` provides a slightly better RMSE as the algorithms `ChargeFixedInterpolation_TimeHalfMax` or `ChargeFixedSpline_TimeHalfMax` but a longer optimal window is necessary. Especially for shortly varying NSB rates the smallest possible window is to be chosen.

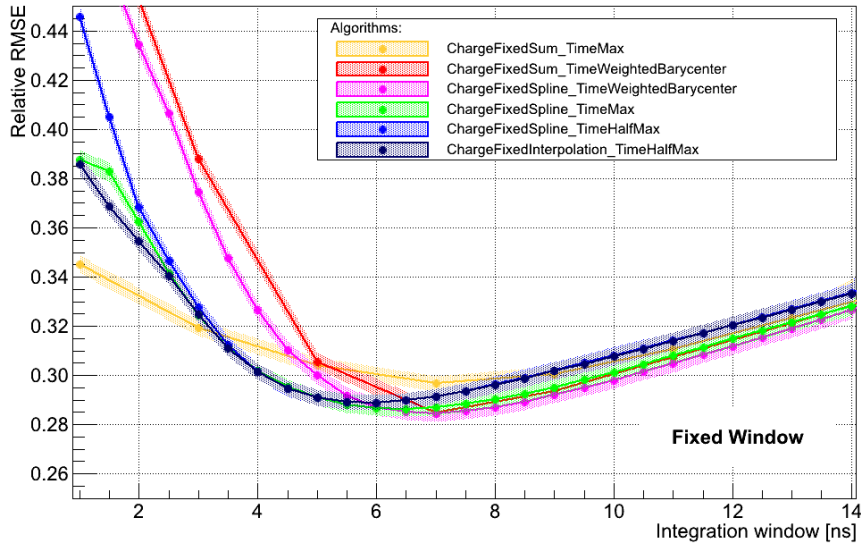


Figure 5.5.: Relative RMSE as a function of the integration window for algorithms using the window method Fixed. Readout samples with 1xNSB and $S_{true} = 5$ p.e. have been used.

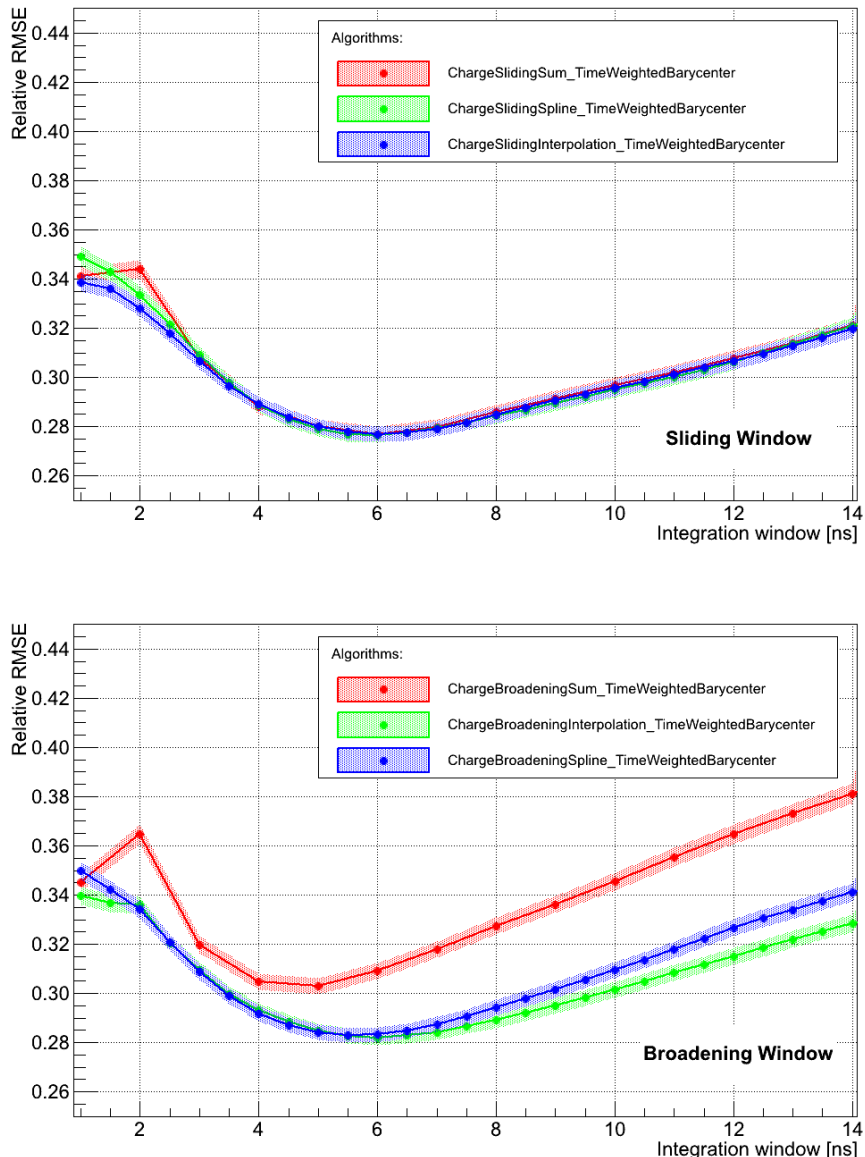


Figure 5.6.: Relative RMSE as a function of the integration window for algorithms using the window methods Sliding (top) and Broadening (bottom). Readout samples with 1xNSB and $S_{true} = 5$ p.e. have been used.

Comparison of Telescope Sizes

In Figure 5.7 the RMSE for diverse values of S_{true} and the three telescope types SST, MST and LST is plotted. The resolution improves for increasing Cherenkov signals while the optimal integration window extends. This is referred to the cause that Cherenkov signals of a higher energy vary more significantly from signals of NSB photons and the charge is extracted more precisely. On the other hand, the pulse shape broadens with increasing energy which requires accordingly a longer integration window.

A comparison of the resolution between the three telescope types shows that the best resolution and the shortest optimal window is obtained with a LST. As these large-size telescopes are designed in particular for the detection of low-energy gamma-rays with a preferably high sensitivity, the obtained result is hugely satisfying.

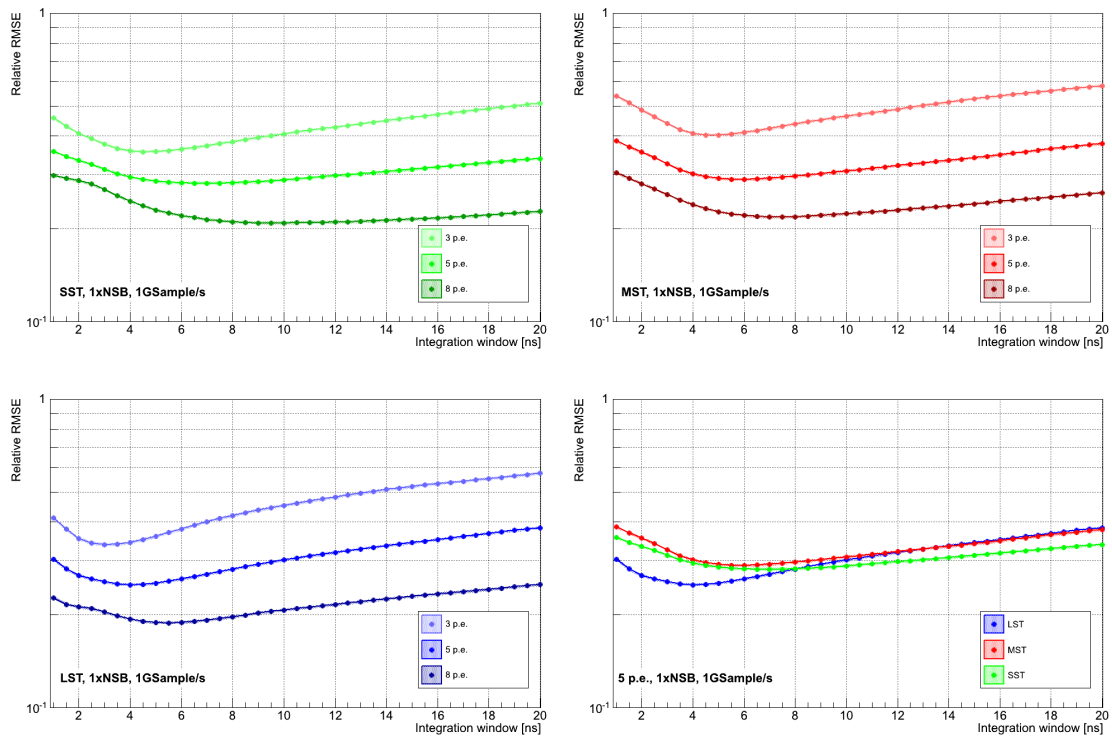


Figure 5.7.: Relative RMSE to compare different telescope sizes as a function of the integration window. The influence of diverse values of S_{true} is illustrated for the three telescope types SST (top left), MST (top right) and LST (bottom left) using the example of the algorithm `ChargeFixedInterpolation_TimeHalfMax`. Additionally, the RMSE for $S_{true} = 5\text{ p.e.}$ is shown for all telescope sizes in one plot (bottom right). Readout samples with 1xNSB and a sampling rate of 1 GSample/s have been used.

Comparison of NSB rates

Figure 5.8 depicts the RMSE for one-times (1xNSB) and four-times (4xNSB) an assumed NSB rate for the three telescope types and for diverse values of S_{true} . The assumed NSB rate amounts to 0.121 p.e./ns per pixel of a LST or MST camera and 0.08464 p.e./ns per pixel of a SST camera.

The resolution worsens for higher NSB rates which is easily comprehensible since the probability to extract NSB photons rises. Additionally, it shows once more very plainly the importance of small integration windows, especially in the presence of increased NSB.

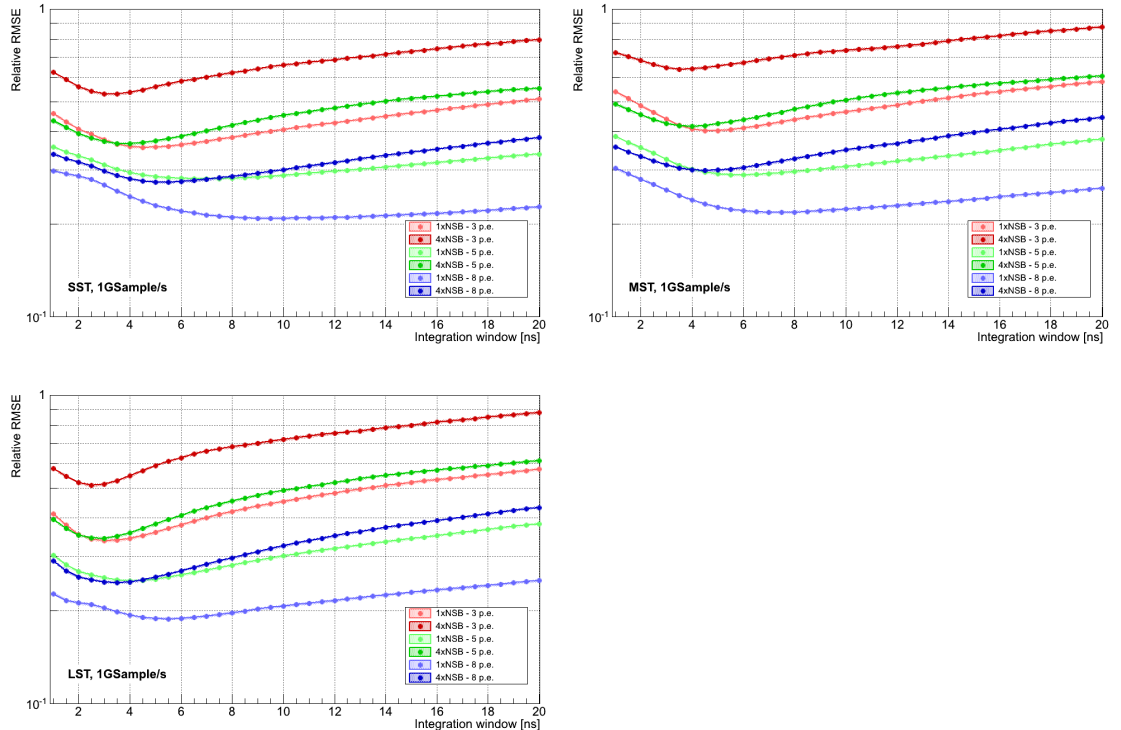


Figure 5.8.: Relative RMSE to compare different NSB rates as a function of the integration window. The influence of diverse values of S_{true} is illustrated for the three telescope types SST (top left), MST (top right) and LST (bottom left) using the example of the algorithm ChargeFixedInterpolation_TimeHalfMax. Readout samples with a sampling rate of 1 GSample/s have been used.

Comparison of Sampling Rates

The comparison between sampling rates of 250 MSample/s and 1 GSsample/s for different values of S_{true} and two NSB rates is illustrated in Figure 5.9. Since fixed window methods are not suited for low sampling rates due to the implicated small resolution of the pulse shape, the RMSE is determined using the example of the algorithm `ChargeSlidingSpline_TimeWeightedBarycenter`.

In general, readout samples with a sampling rate of 250 MSample/s result in a worse RMSE than readout samples with a sampling rate of 1 GSsample/s. The RMSE is nearly constant over the integration time for the small sampling rate which is referred to the cause that the corresponding readout samples consist of fewer and wider time slices. Consequently, the shape of the pulse is not well defined. Since an optimal window is not clearly recognizable, a window of roughly 2 ns seems reasonable for the low sampling rate. In case of the nominal NSB rate and small integration windows, the low sampling rate provides a better resolution because the major part of the pulse's information is contained in one slice of 4 ns and the sliding window extracts in this range simply fractions of this important slice.

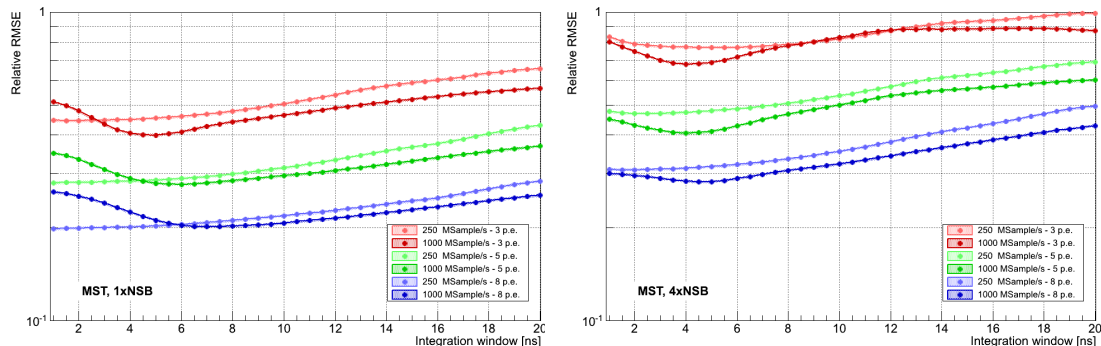


Figure 5.9.: Relative RMSE to compare different sampling rates as a function of the integration window. The influence of diverse values of S_{true} is illustrated for 1xNSB (left) and 4xNSB (right) using the example of the algorithm `ChargeSlidingSpline_TimeWeightedBarycenter`. Readout samples simulated for a MST have been used.

5.6. Results and Comparisons concerning the Arrival Time Extraction

Figure 5.10 and Figure 5.11 depict the mean and the RMS of different algorithms to extract the arrival time information. In contrast to the previous sections, the RMS is used instead of the RMSE to evaluate the quality of a given extractor. The calculation of the RMSE according to Equation 4.8 requires the bias which indicates the deviation between the obtained and the intended arrival time. But since no intended arrival time information is available, the RMS equivalent to the standard deviation is chosen.

Algorithms using the position of the maximum or the position of the half maximum at the rising edge feature a constant mean as well as a constant RMS because these positions are independent of the integration window. In contrast, algorithms using the position of the signal-weighted barycenter depend on the position and the width of the integration window and thus they are not constant. Particularly the RMS shows variations depending on the integration window.

While the mean of all algorithms is constant, the mean of the algorithm using a broadening window deviates more and more from a constant value for increasing integration windows. This algorithm implicates an integration window which is broadening firstly to both sides but then it is broadening to the right side, once a minimum at the left side is reached. For this reason, the window for the signal-weighted barycenter is moving from a certain moment on only in one direction which explains the abnormality of the mean.

The algorithm `ChargeFixedSpline_TimeWeightedBarycenter` provides the smallest optimal integration window and the best RMS since the weighting is performed with a fine resolution and the spline corrects for fluctuations and forms and smooths the pulse shape. The remaining algorithms using the position of the signal-weighted barycenter feature an optimal integration window around 6 – 10 ns.

The RMS of the algorithm using a sliding window is decreasing a second time subsequent to a rise. The first minimum is obtained when the sliding window is adjusted to one single pulse. The maximum RMS contains events where parts of two single pulses were combined as shown in Figure 4.6. Subsequently, larger windows compensate this effect.

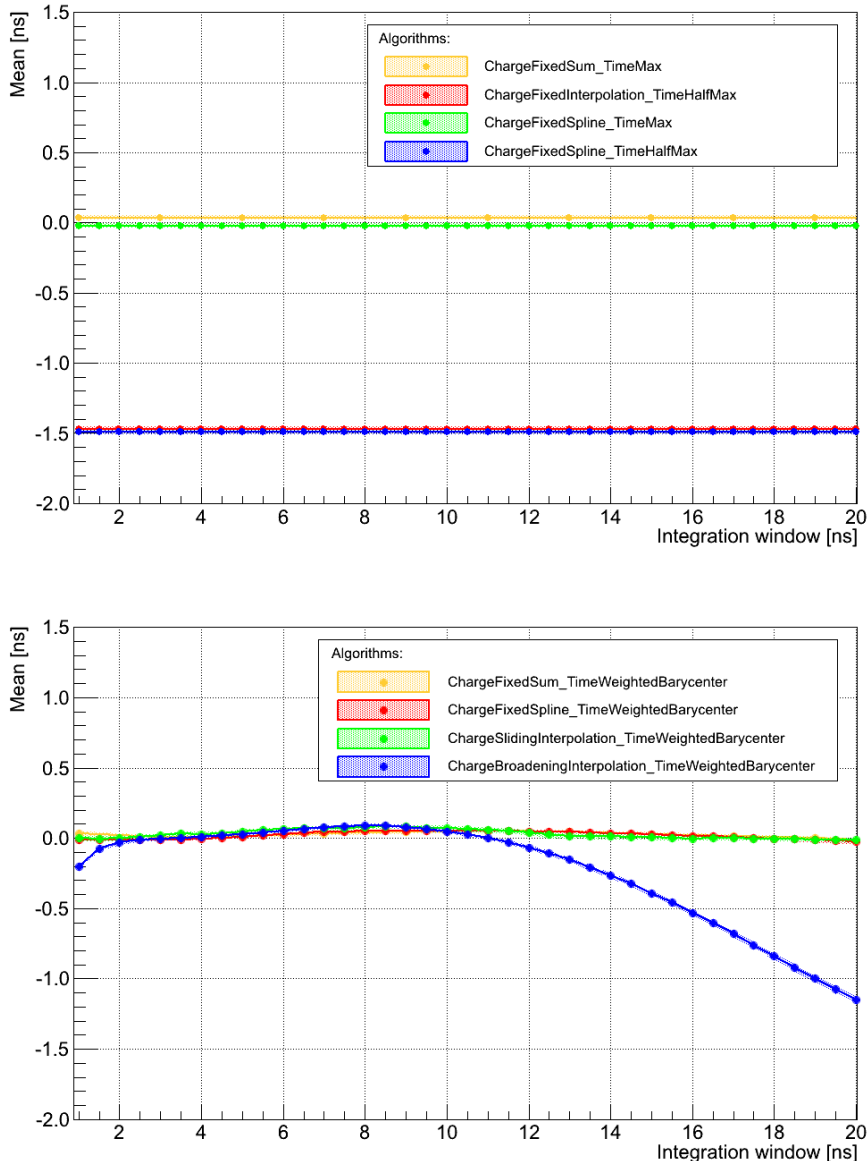


Figure 5.10.: Mean of the extracted arrival time using different algorithms as a function of the integration window. They are ordered by WeightedBarycenter algorithms (bottom) and Max and HalfMax algorithms (top). Readout samples with 1xNSB and a sampling rate of 1 GSsample/s have been used.

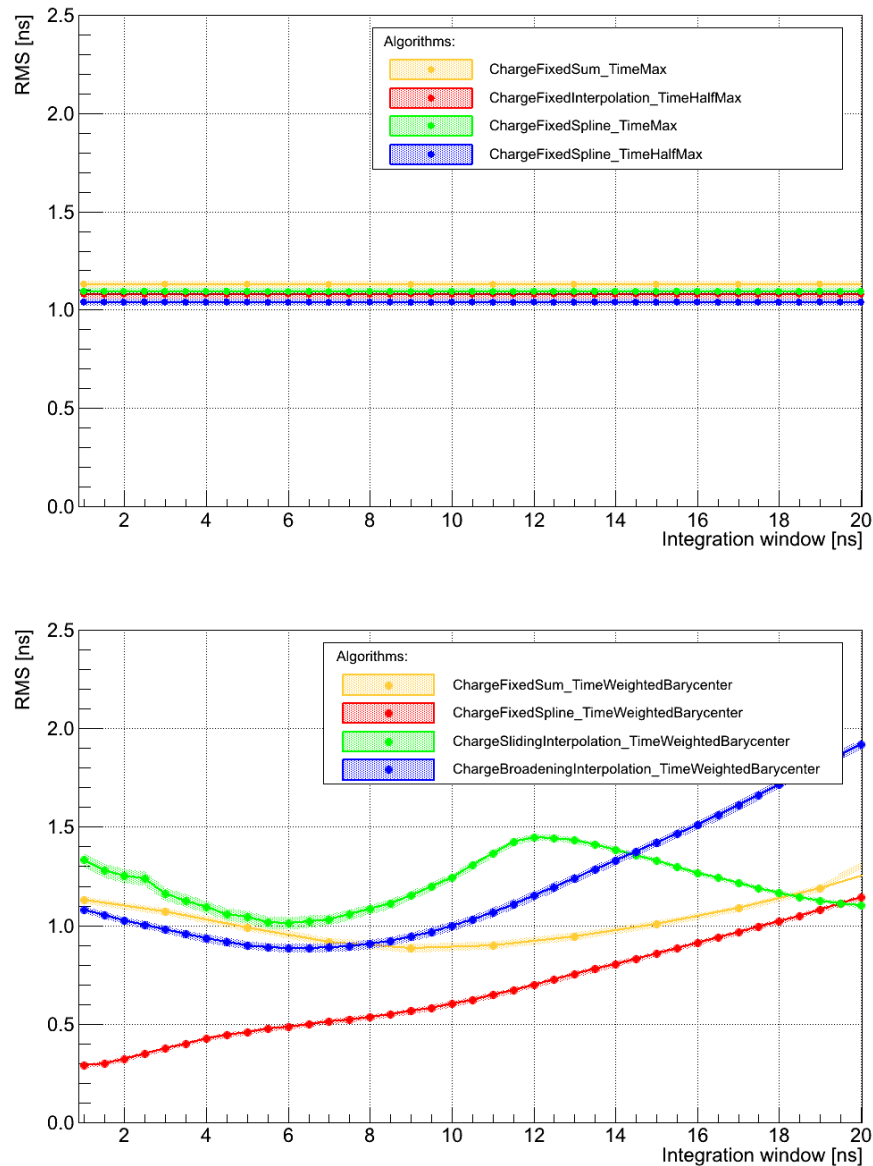


Figure 5.11.: RMS of the extracted arrival time using different algorithms as a function of the integration window. They are ordered by WeightedBarycenter algorithms (bottom) and Max and HalfMax algorithms (top). Readout samples with 1xNSB and a sampling rate of 1GSample/s have been used.

6. Signal Extraction Study for FACT

This chapter addresses a similar study of the signal extraction as the previous chapter. The study is performed for the FACT project and covers also the high-energy regime. Since FACT is already operating, a comparison of different configuration parameters is unnecessary and only the influences of various physical parameters are examined. Appropriate Monte Carlo simulations, as described in section 6.1, are developed and adjusted to the properties of FACT. Empirical chosen algorithms are applied to these generated readout samples. The subsequent sections constitute results of the calibration and the extraction.

6.1. Monte Carlo simulation of the readout samples

In order to have appropriate MCs for this study, a small framework was written by D. Neise (TU Dortmund) simulating the readout samples in a straight-forward approach with several simplified assumptions.

Within this framework, a pulse template is used to simulate the NSB photons by placing it to random positions at an indicated rate. Assuming a stable NSB rate, the mean over all time slices of a readout sample which contains only NSB photons should equal 0 due to the AC coupling. On this account the baseline is adjusted by subtracting this mean. Subsequently, the pulse template is scaled to a user-defined number of photoelectrons serving as the Cherenkov signal. It is placed at a user-defined position varied with a Gaussian distribution due to the telescope's time resolution of about 600ps. Afterwards, every time slice is smeared out and a Gaussian distributed electronic noise with a user-defined standard deviation is added.

The pulse template was determined by J. Buss (TU Dortmund) in the course of his diploma thesis, see [52]. Therefore, so-called dark counts were measured during the camera was closed. Dark counts are pulses induced by thermal excitation within the semi-conductor which produce a similar pulse shape as photons due to the same physical process during the measurement. The advantage of using data acquired with a closed camera is the small noise contamination. Pulses with the same content of photoelectrons were stacked at a defined position and fitted with the function

$$U(t) = B + A_0 \cdot \Theta(t - t_0) \left(1 - e^{-\frac{t-t_0}{\tau_1}}\right) \cdot \left(e^{-\frac{t-t_0}{\tau_2}}\right) \quad (6.1)$$

which corresponds to a charging curve of a parasitic capacity and a discharging curve of the depletion layer with the time constants τ_1 and τ_2 [53]. The other parameters describe the baseline B , the time t_0 when the avalanche starts and the asymptote A_0 of the charging curve. The result of the fit of single photons is used as the above mentioned template.

The nominal NSB contribution is estimated with a rate of 0.03 p.e./ns per pixel while the electronics noise contribution is adjusted to 3.6 mV. This value is determined by random-triggered data recorded during the shutter of the camera was closed to avoid additional noise contribution by the NSB. Additionally, it is supposed that signals scale linearly with the number of photoelectrons.

Figure 6.1 gives an example of a simulated readout sample. The Cherenkov signal as well as NSB photons can be identified well. Figure 6.2 compares a simulated readout sample with a real sample recorded during a dark night. The pulse shape of the real sample seems to be wider with longer time constants as the fitted ones.

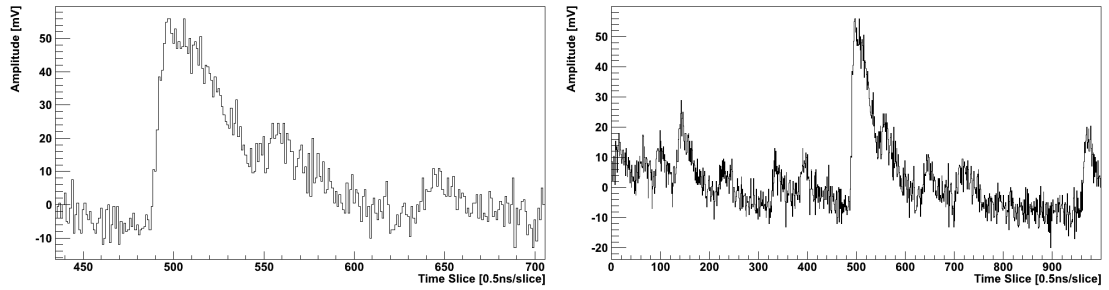


Figure 6.1.: Example of a simulated readout sample with a Cherenkov signal of $S_{true} = 5$ p.e. and a nominal NSB rate. The sample is shown in constraint range (left) and in the whole range with a duration of 500 ns (right).

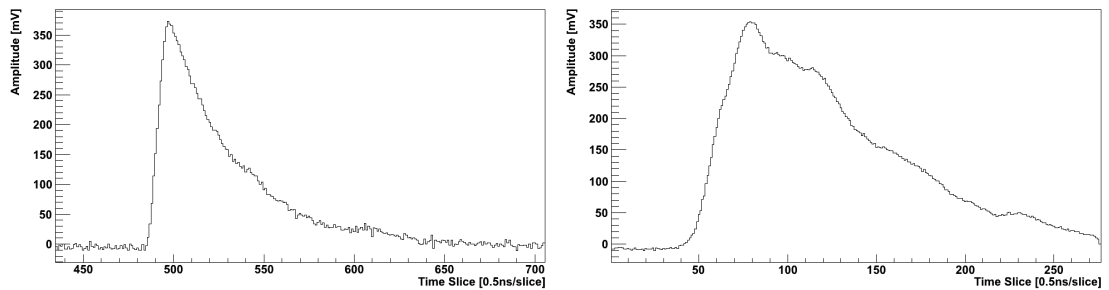


Figure 6.2.: Comparison between a simulated (left) and a real (right) readout sample. The simulated one contains a Cherenkov signal of $S_{true} = 30$ p.e. and a nominal NSB rate while the real sample was recorded in a dark night.

6.2. Calibration

The determination of a calibration factor is necessary to convert integrated signals with diverse integration windows and algorithms to the intended number of photoelectrons. Figure 6.3 illustrates the obtained factors for different combinations of ranges and integration windows using the example of the algorithm `ChargeFixedSum_TimeMax`. The factors and their corresponding errors determined for the lowest number of photoelectrons deviate differently from the constant factor depending on the combination of the range, the integration window and the NSB rate.

The less NSB contribution, the smaller is the error and the lower is the limit for a constant factor because the probability to extract mistakenly a NSB photon decreases with decreasing NSB contribution. This confirms also the decisions for the estimation of the calibration factor in section 5.2.

Concerning the choice of the range, a small range is preferable since it approaches earlier a constant although the implicated error is larger.

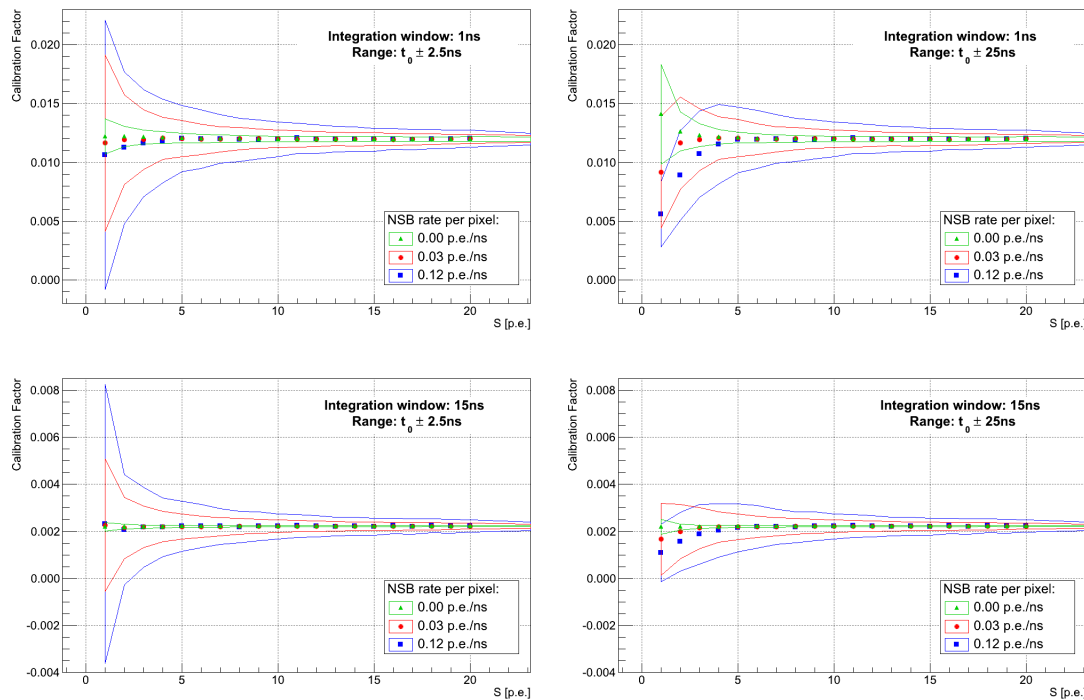


Figure 6.3.: Influence of range and integration window on the calibration factor as a function of the NSB rate. In order to calculate the factor, the algorithm `ChargeFixedSum_TimeMax` is applied to readout samples in the ranges $t_0 \pm 2.5\text{ ns}$ (left) and $t_0 \pm 25\text{ ns}$ (right) with integration windows of 1 ns (top) and 15 ns (bottom).

6.3. Results and Comparisons concerning the Charge Extraction

This section will compare various adjustment parameters, distinct physical parameters and empirical chosen algorithms with each other. Additionally, results of the obtained resolution regarding the charge extraction dependent on the number of photoelectrons are shown.

Comparison of Ratios

The fixed window algorithms require the adjustment of a ratio which has to be adapted to the electronics specific pulse shape. Typically, G-APD pulse shapes of variable number of photoelectrons differ mainly in the pulse height while the pulse width and the time constants are constant. Since the charging time constant is much shorter than the discharging one, the ratio should be around $\frac{\tau_1}{\tau_2} \approx 0.15$.

As expected, the resolution and its error for no NSB contribution are the best and worsen with more noise. The resolution obtained with a ratio of 0.2 provides the best results both for readout samples with NSB contributions and samples with different Cherenkov signals.

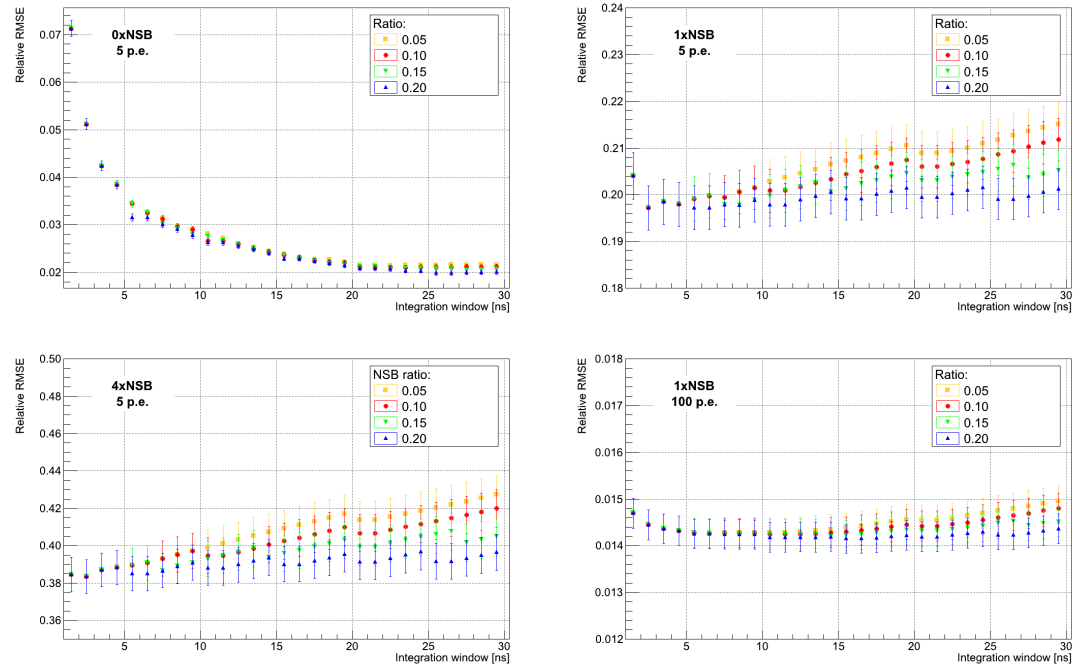


Figure 6.4.: Relative RMSE in order to adjust the ratio using the example of the algorithm `ChargeFixedSum_TimeWeightedBarycenter`. The influence of diverse NSB rates and S_{true} are shown as well.

Comparison of NSB rates

Figure 6.5 depicts the dependencies of the NSB rate for the algorithm `FixedSum` as it is implemented in the newly developed analysis software PARFACT [54]. Within this algorithm, an integration window of 15ns starts at the position of the half maximum at the rising edge. Since the integration window in PARFACT is chosen only intuitive, an examination if alternative integration windows helps to determine an optimized window. Simulations with $S_{true} = 5$ p.e. suggest a smaller window while simulations with $S_{true} = 100$ p.e. recommend a window between 15 and 20 ns as afterwards the resolution improves only slightly.

Figure 6.6 illustrates more or less constant resolutions without a clear optimal window. Due to a kind of an optimizing self-adjustment, the algorithms corrects for fluctuations.

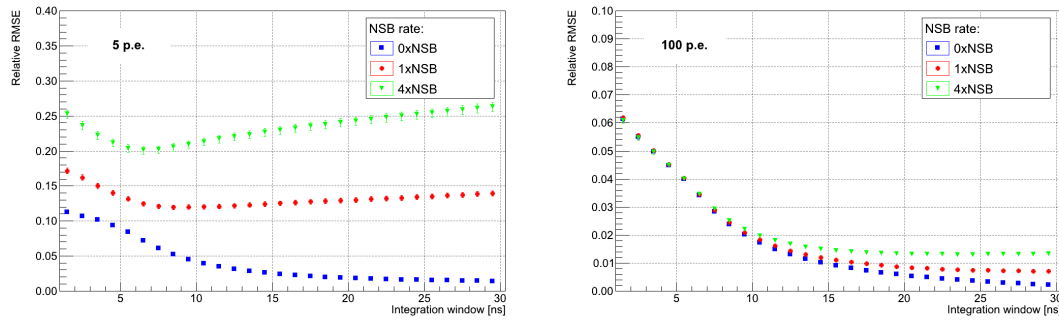


Figure 6.5.: Relative RMSE for different NSB rates and S_{true} using the example of the algorithm `FixedSum`. The integration window is positioned analogous to PARFACT [54].

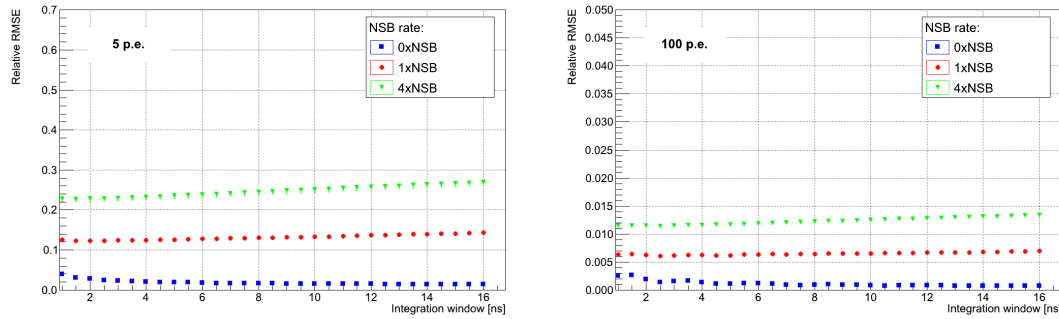


Figure 6.6.: Relative RMSE for different NSB rates and S_{true} using the example of the algorithm `SlidingSum`.

Comparison of the Algorithms

Figure 6.7 makes a direct comparison between the chosen algorithms for different combinations of NSB rate and S_{true} . According to that, the algorithm `FixedSum` around the signal-weighted barycenter is only suitable to a limited extent. The both other algorithms provide much better results. While the sliding window algorithm features a stability over time, the fixed window algorithm starting from the position of the half maximum provides better resolutions for certain integration windows.

The resolution of these both algorithms is now to be determined as a function of the number of photoelectrons. Figure 6.8 and Figure 6.9 show the obtained results for different NSB rates and various integration windows which has been discusses previously. The stability of the algorithm `SlidingSum` is apparent again but this time concerning the integration window. In contrast, the algorithm `FixedSum` depends on the integration window, especially in the high-energy regime. Subject to the number of photoelectrons, integration windows between 10 and 15ns seems reasonable. Larger integration windows improve only slightly but the signal-to-noise ratio worsens.

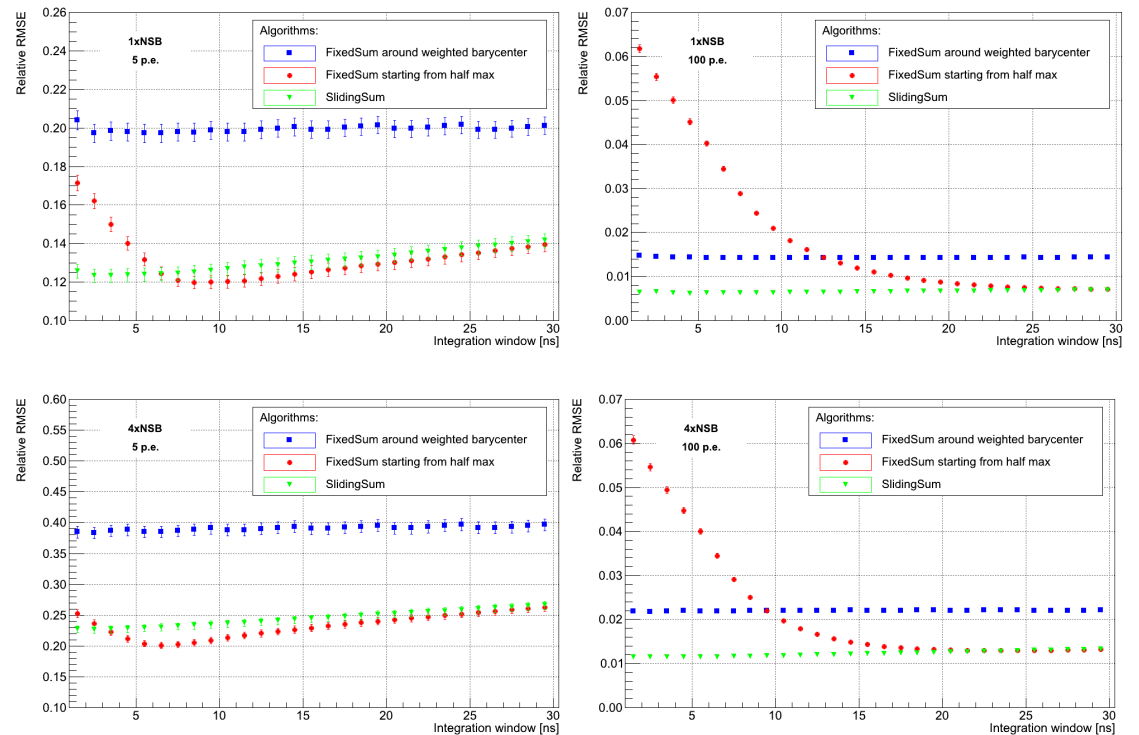


Figure 6.7.: Relative RMSE of the empirical chosen algorithms in a direct comparison for 1xNSB (top) and 4xNSB (bottom) and $S_{true} = 5$ p.e. (left) and $S_{true} = 100$ p.e. (right).

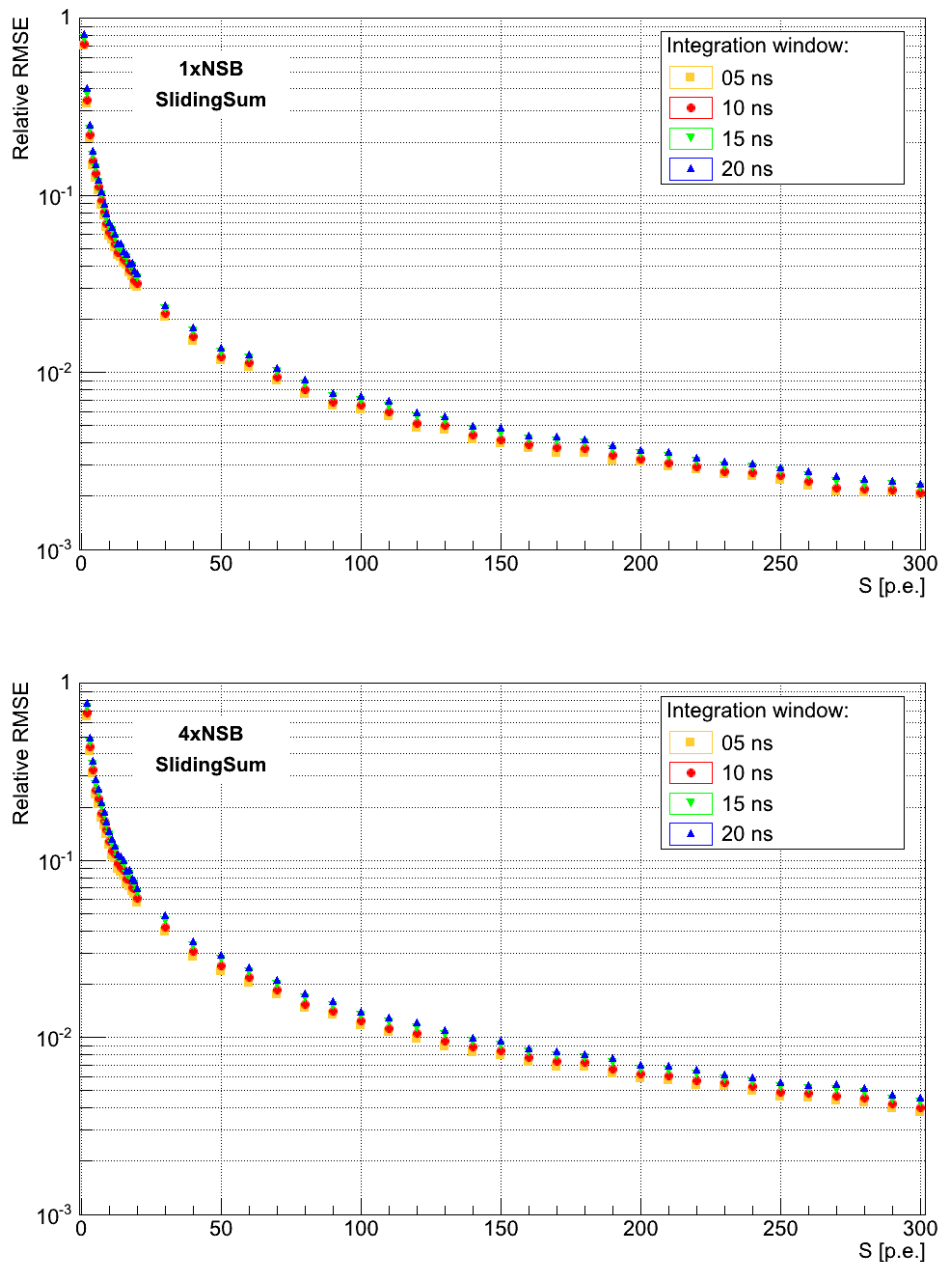


Figure 6.8.: Relative RMSE for different integration windows as a function of the number of photoelectrons using the example of the algorithm SlidingSum. Readout samples with 1xNSB (top) and 4xNSB (bottom) have been used.

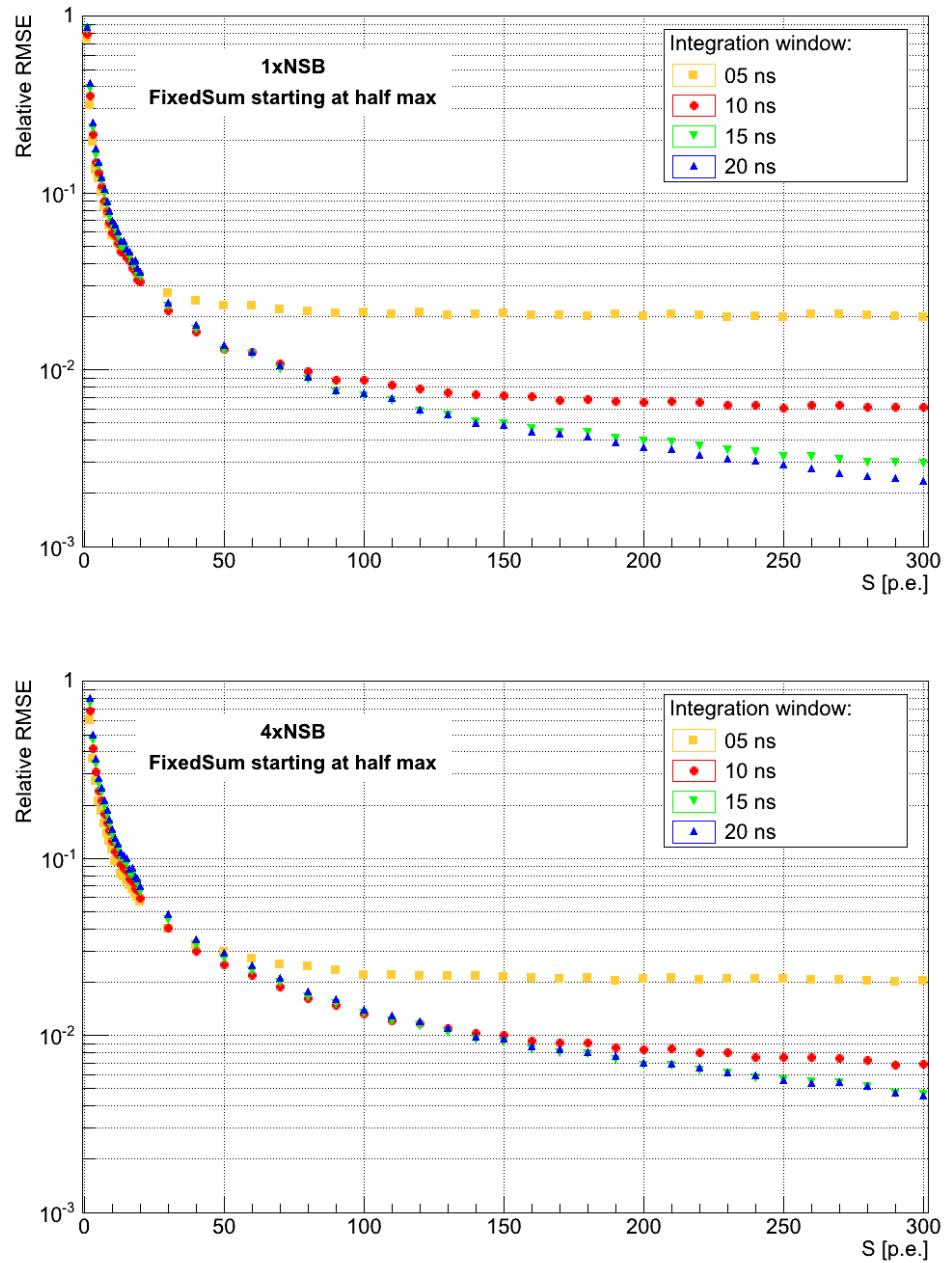


Figure 6.9.: Relative RMSE for different integration windows as a function of the number of photoelectrons using the example of the algorithm FixedSum starting at the position of the half maximum. Readout samples with 1xNSB (top) and 4xNSB (bottom) have been used.

7. Conclusion and Outlook

7.1. Conclusion

The scope of this thesis was to study the extraction of the charge and arrival time information from the readout samples regarding the obtainable resolution for different physical and configuration parameters. Subsequent to a general introduction of extraction algorithms and the needed methods for that, the algorithms have been implemented in several classes which allow not only an easy application to other programs but also further extensions. Additionally, multiple functions for an easy adjustment of values and for the purpose of analyzing and debugging have been integrated. Advanced algorithms as well as requirements to the algorithms complete the description of the algorithms. In order to evaluate them, a number of evaluation criteria have been carried out.

Concerning the study performed for the future experiment CTA, the following steps have been accomplished: An estimation of the calibration factor has been determined as well as an optimization with regards to the adjustment of the range and the ratio. The range has been adjusted to $t_0 \pm 5\text{ns}$ for all algorithms but the ones using a sliding window. For these algorithms the range has been adjusted to $t_0 \pm 10\text{ns}$. The values regarding the ratio have been determined dependent on the calculation of the arrival time. For methods using the position of the signal-weighted barycenter a ratio of 0.5 has been chosen while a ratio of 0.45 for the maximum position method and a ratio of 0.2 for the position of the half maximum method has been most suitable. Furthermore, several comparisons concerning the charge extraction have been presented. The comparison of the window methods led to sliding window algorithms while the examination of integration methods showed similar results for the interpolation and spline integration. In this context, algorithms using the half maximum at the rising edge to position the integration window could have been suggested. Regarding different telescope types, the best resolution and the smallest optimal window have been obtained for a large-size telescope which is very likely since these telescopes are particularly designed for the low-energy regime. As a matter of course, the resolution of the signal extraction worsens in the presence of an increased NSB rate wherefore smaller integration windows are required to keep a high signal-to-noise ratio. Especially the sampling rate of the readout system related to the consideration between performance and costs is of interest. But it has been turned out that improved and optimized algorithms are not able to compensate slower electronics and a sampling rate of 1 GSsample/s is necessary to achieve the intended resolution and sensitivity for CTA. The comparison drawn for the arrival time extraction, appreciated the algorithm `ChargeFixedSpline_TimeWeightedBarycenter` best. For the remaining algorithms an integration window between 6 and 10ns is recommended to extract the arrival time.

Concerning the study performed for the already operating FACT project, the following tasks have been coped as well as the subsequently described results have been obtained: The simulation program required some values for the adaption to the properties of FACT. For this purpose, appropriate values for the NSB rate and the electronics noise have been determined and also the simulation itself has been enhanced. In this context, the simulated samples have been compared to real samples and differences regarding the rising edge and the slope have been turned out. Nevertheless, a large amount of readout samples has been generated for several NSB rates and number of photoelectrons. Calibration factors also for a larger number of photoelectrons as in the CTA study have been determined and confirmed the estimation for CTA. Empirical chosen algorithms which seemed to be appropriate for the FACT study were applied and comparisons have been made. In this way, the ratio has been adjusted to 0.2 and the algorithm `ChargeFixedSum_TimeWeightedBarycenter` has been discarded for FACT. With a view to the resolution of the remaining algorithms as a function of the number of photoelectrons and the integration window, a recommended integration window for the algorithm used within the newly developed analysis software PARFACT has been determined to 10 – 15 ns.

7.2. Outlook

Based on the conducted study, the obtained results and previously described conclusions, further steps are suggested as follows:

- The conducted CTA study should be enlarged to higher energies to examine the capability of the obtained results.
- Another idea, as already proposed in CTA collaboration meetings, uses a dynamic integration window which adjusts the integration window according to the amplitude. This would enhance the resolution further.
- The proposed advanced algorithms taking all pixels and the information of the arrival time along the shower axis into account should be implemented, tested and optimized. Furthermore, the basic algorithms studied in this thesis could be embedded in existing software tools.
- Moreover, the reason why the simulated readout samples for FACT differ from real samples to that extent has to be found and subsequently the simulation has to be improved and repeated.

A. Appendix

Used files for the CTA study

```
PixelData_gamma_T1e0E10000p0P10000_B1_D3TK3125q3Q3W50.root
PixelData_gamma_T1e0E10000p0P10000_B1_D3TK3125q5Q5W50.root
PixelData_gamma_T1e0E10000p0P10000_B1_D3TK3125q8Q8W50.root
PixelData_gamma_T2e0E10000p0P10000_B1_D3TK3125q3Q3W50.root
PixelData_gamma_T2e0E10000p0P10000_B1_D3TK3125q5Q5W50.root
PixelData_gamma_T2e0E10000p0P10000_B1_D3TK3125q8Q8W50.root
PixelData_gamma_T3e0E10000p0P10000_B1_D3TK3125q3Q3W50.root
PixelData_gamma_T3e0E10000p0P10000_B1_D3TK3125q5Q5W50.root
PixelData_gamma_T3e0E10000p0P10000_B1_D3TK3125q8Q8W50.root
PixelData_gamma_T1e0E10000p0P10000_B4_D3TK3125q3Q3W50.root
PixelData_gamma_T1e0E10000p0P10000_B4_D3TK3125q5Q5W50.root
PixelData_gamma_T1e0E10000p0P10000_B4_D3TK3125q8Q8W50.root
PixelData_gamma_T2e0E10000p0P10000_B4_D3TK3125q3Q3W50.root
PixelData_gamma_T2e0E10000p0P10000_B4_D3TK3125q5Q5W50.root
PixelData_gamma_T2e0E10000p0P10000_B4_D3TK3125q8Q8W50.root
PixelData_gamma_T3e0E10000p0P10000_B4_D3TK3125q3Q3W50.root
PixelData_gamma_T3e0E10000p0P10000_B4_D3TK3125q5Q5W50.root
PixelData_gamma_T3e0E10000p0P10000_B4_D3TK3125q8Q8W50.root
PixelData_gamma_T1e0E10000p0P10000_B1_D5TK3125q3Q3W50.root
PixelData_gamma_T1e0E10000p0P10000_B1_D5TK3125q5Q5W50.root
PixelData_gamma_T1e0E10000p0P10000_B1_D5TK3125q8Q8W50.root
PixelData_gamma_T2e0E10000p0P10000_B1_D5TK3125q3Q3W50.root
PixelData_gamma_T2e0E10000p0P10000_B1_D5TK3125q5Q5W50.root
PixelData_gamma_T2e0E10000p0P10000_B1_D5TK3125q8Q8W50.root
PixelData_gamma_T3e0E10000p0P10000_B1_D5TK3125q3Q3W50.root
PixelData_gamma_T3e0E10000p0P10000_B1_D5TK3125q5Q5W50.root
PixelData_gamma_T3e0E10000p0P10000_B1_D5TK3125q8Q8W50.root
PixelData_gamma_T1e0E10000p0P10000_B4_D5TK3125q3Q3W50.root
PixelData_gamma_T1e0E10000p0P10000_B4_D5TK3125q5Q5W50.root
PixelData_gamma_T1e0E10000p0P10000_B4_D5TK3125q8Q8W50.root
PixelData_gamma_T2e0E10000p0P10000_B4_D5TK3125q3Q3W50.root
PixelData_gamma_T2e0E10000p0P10000_B4_D5TK3125q5Q5W50.root
PixelData_gamma_T2e0E10000p0P10000_B4_D5TK3125q8Q8W50.root
PixelData_gamma_T3e0E10000p0P10000_B4_D5TK3125q3Q3W50.root
```

```
PixelData_gamma_T3e0E10000p0P10000_B4_D5TK3125q5Q5W50.root
PixelData_gamma_T3e0E10000p0P10000_B4_D5TK3125q8Q8W50.root
```

Adjustment of the range considering bias, RMS and RMSE

In the following the algorithms `ChargeFixedSpline`, `ChargeSlidingSpline` and `ChargeBroadeningSpline` are compared considering the relative bias, RMS and RMSE in order to adjust the range.

Bias

Since the bias should equal zero, the smallest range provides the best results for all algorithms and all combinations of NSB rate and S_{true} .

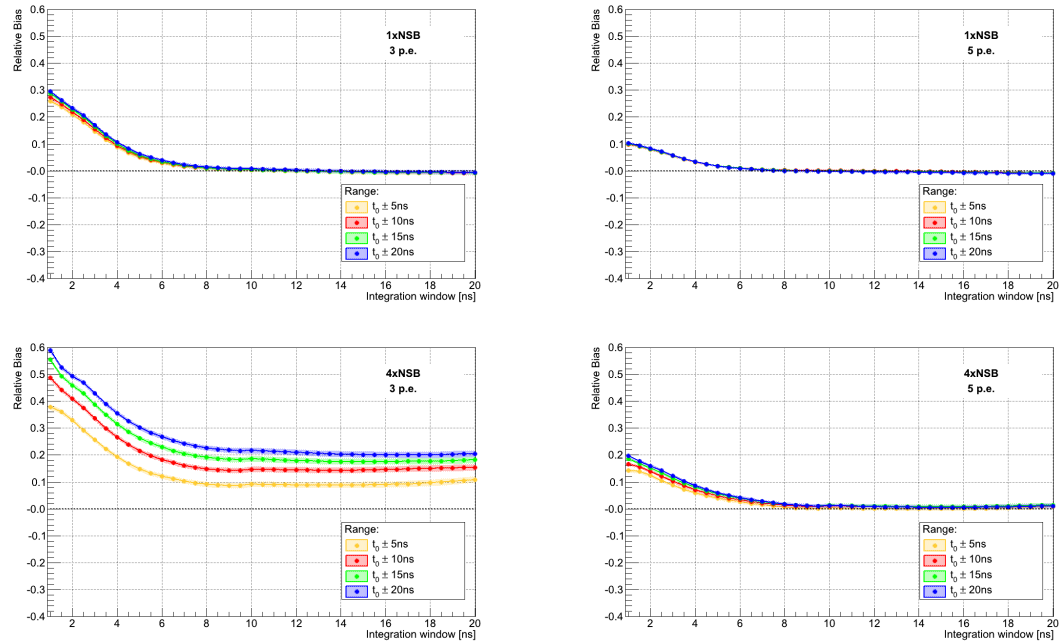


Figure A.1.: Relative bias for a fixed window algorithm as a function of the integration window. The influence of the range relative to the arrival time t_0 for the algorithm `ChargeFixedSpline_TimeMax` is shown for different combinations of NSB rate and number of photoelectrons (p.e.).

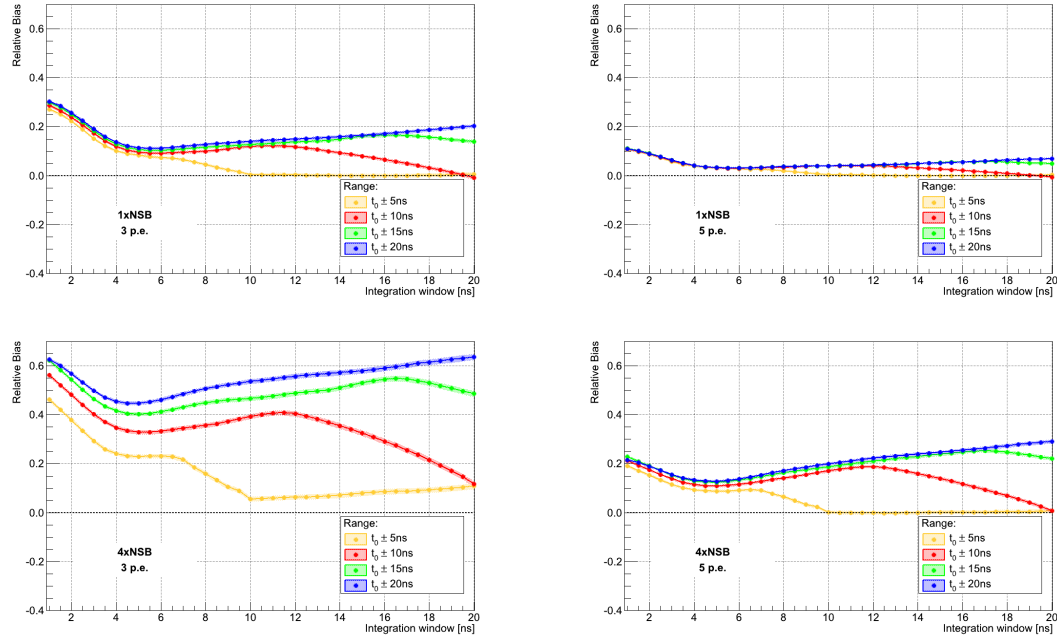


Figure A.2.: Relative bias for the sliding window algorithm ChargeSlidingSpline, analogous to Figure A.1.

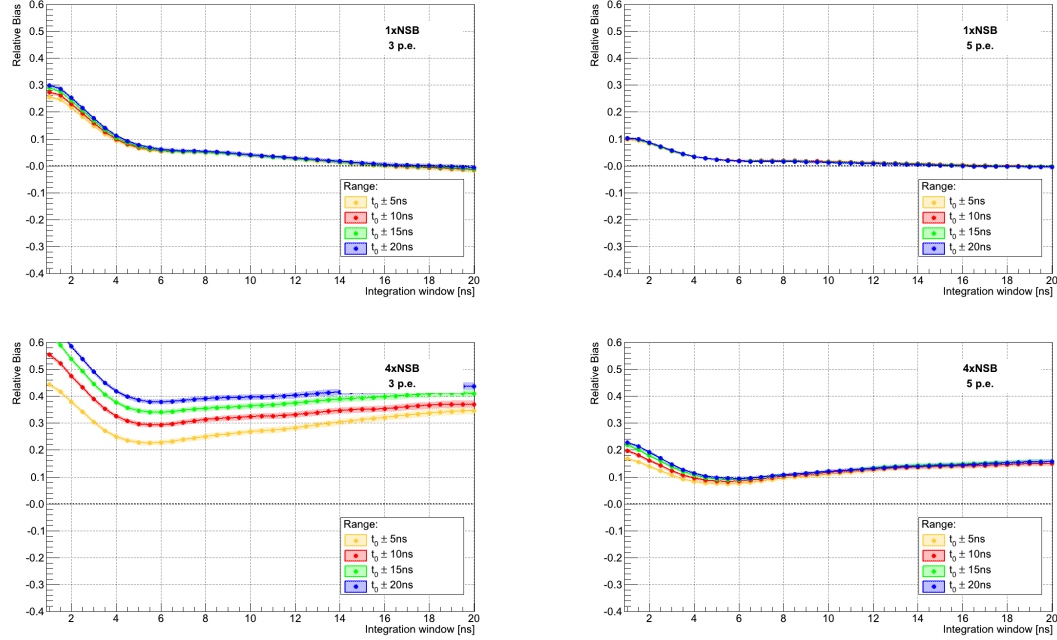


Figure A.3.: Relative bias for the broadening window algorithm ChargeBroadeningSpline, analogous to Figure A.1.

RMS

The value of the RMS should be as small as possible. In this case, the largest range provides the best results for all algorithms and all combinations of NSB rate and S_{true} . Especially for small integration windows the RMS differs for diverse ranges.

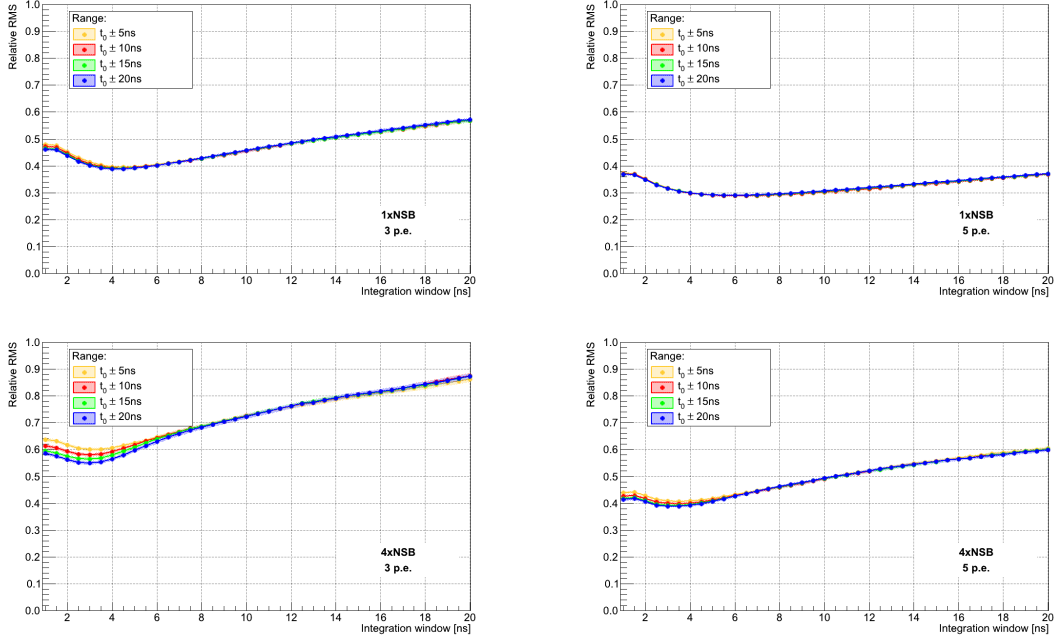


Figure A.4.: Relative RMS for a fixed window algorithm as a function of the integration window. The influence of the range relative to the arrival time t_0 for the algorithm `ChargeFixedSpline_TimeMax` is shown for different combinations of NSB rate and number of photoelectrons (p.e.).

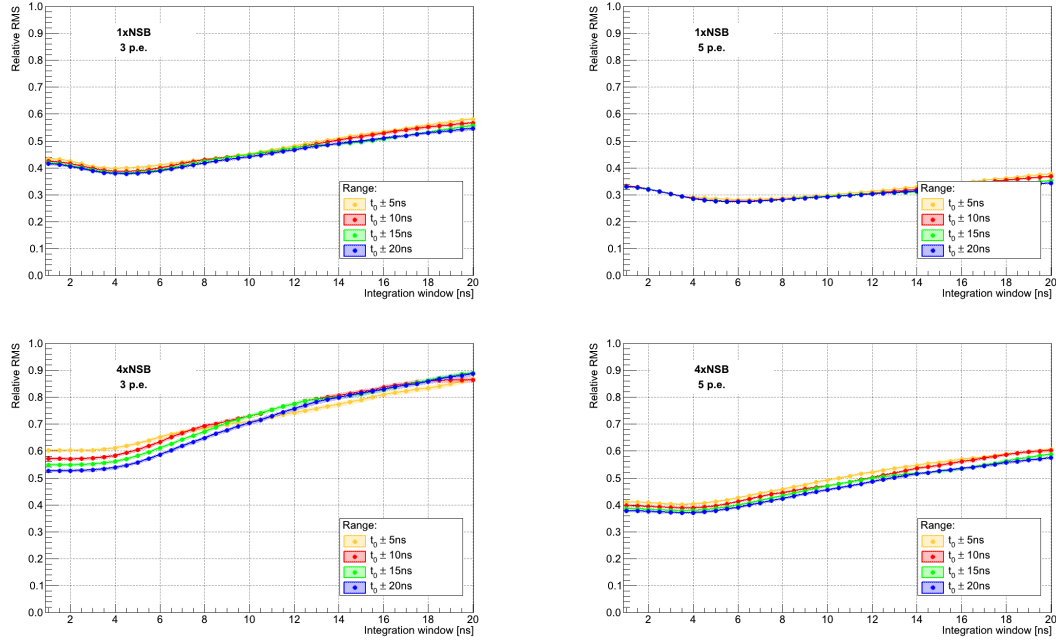


Figure A.5.: Relative RMS for the sliding window algorithm `ChargeSlidingSpline`, analogous to Figure A.4.

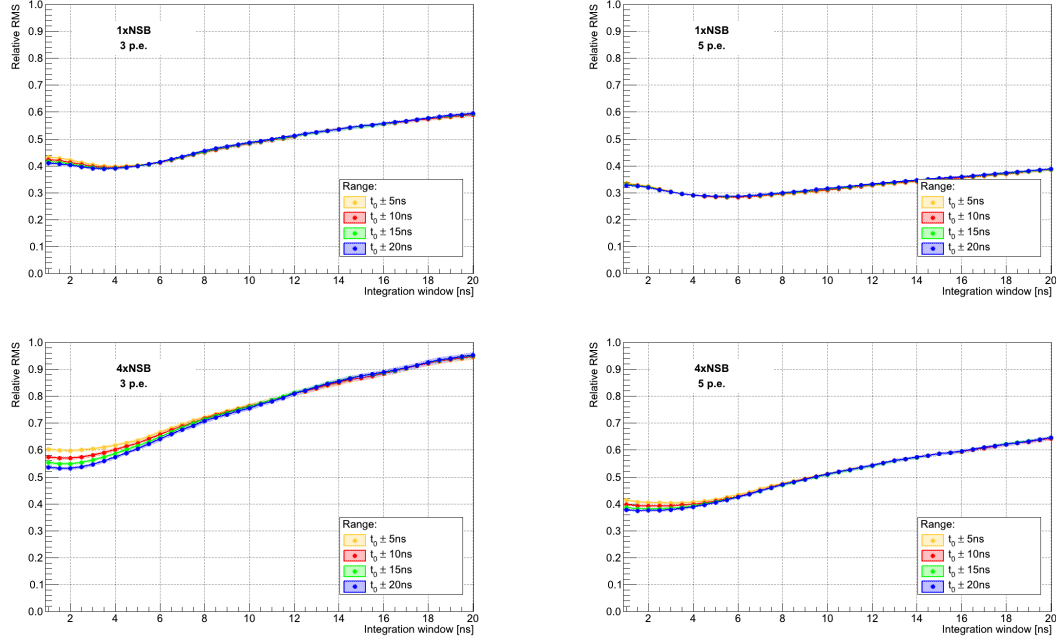


Figure A.6.: Relative RMS for the broadening window algorithm `ChargeBroadeningSpline`, analogous to Figure A.4.

RMSE

The value of the RMSE should be as small as possible as well. Since the RMSE combines the bias and the RMS, it is a trade-off between the best bias and the best RMS or rather between a small range and a large range. Most combinations of algorithm, NSB rate and S_{true} result in very similar values of the RMSE. However, in case of 4xNSB and $S_{true} = 3$ p.e., the smallest range provides the best RMSE more obviously. For that reason and since this study is conducted with regard to the low-energy regime, the range is adjusted to $t_0 \pm 5$ ns for algorithms using a fixed or a broadening window and $t_0 \pm 10$ ns for the sliding window algorithm. Sliding window algorithms require a larger range because in contrast to the remaining algorithms the range is directly used to determine the position of the integration window. The other algorithms use the range only to define the arrival time which subsequently positions the integration window.

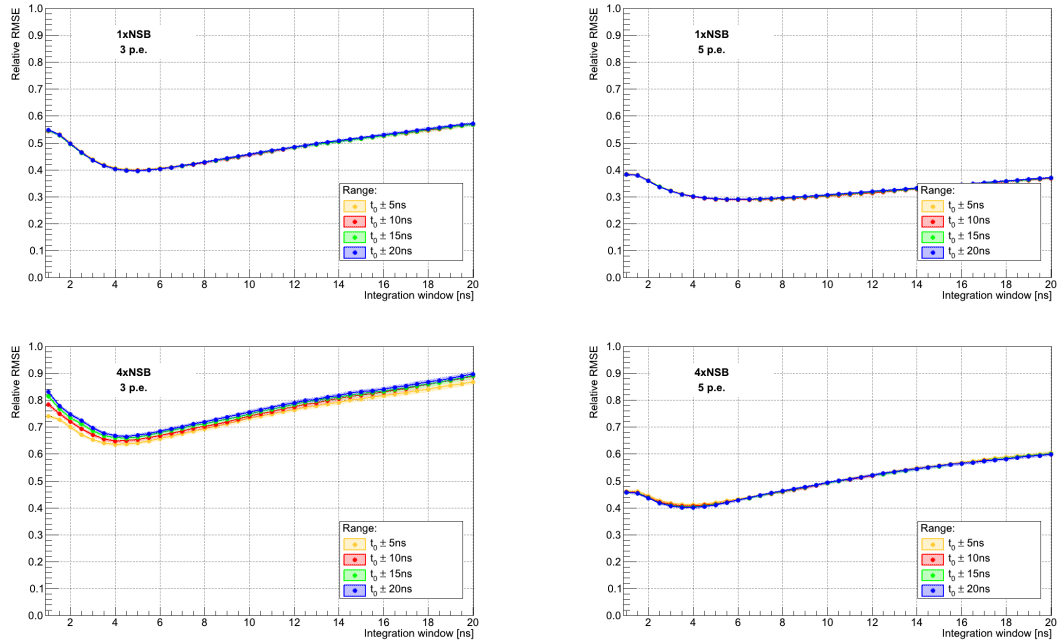


Figure A.7.: Relative RMSE for a fixed window algorithm as a function of the integration window. The influence of the range relative to the arrival time t_0 for the algorithm `ChargeFixedSpline_TimeMax` is shown for different combinations of NSB rate and number of photoelectrons (p.e.).

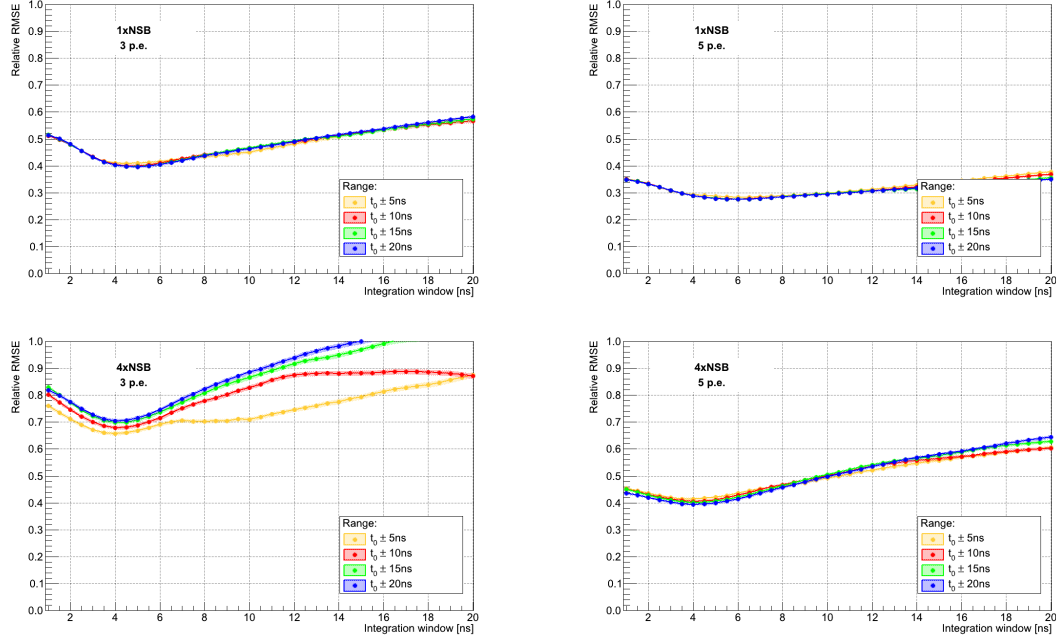


Figure A.8.: Relative RMSE for the sliding window algorithm `ChargeSlidingSpline`, analogous to Figure A.7.

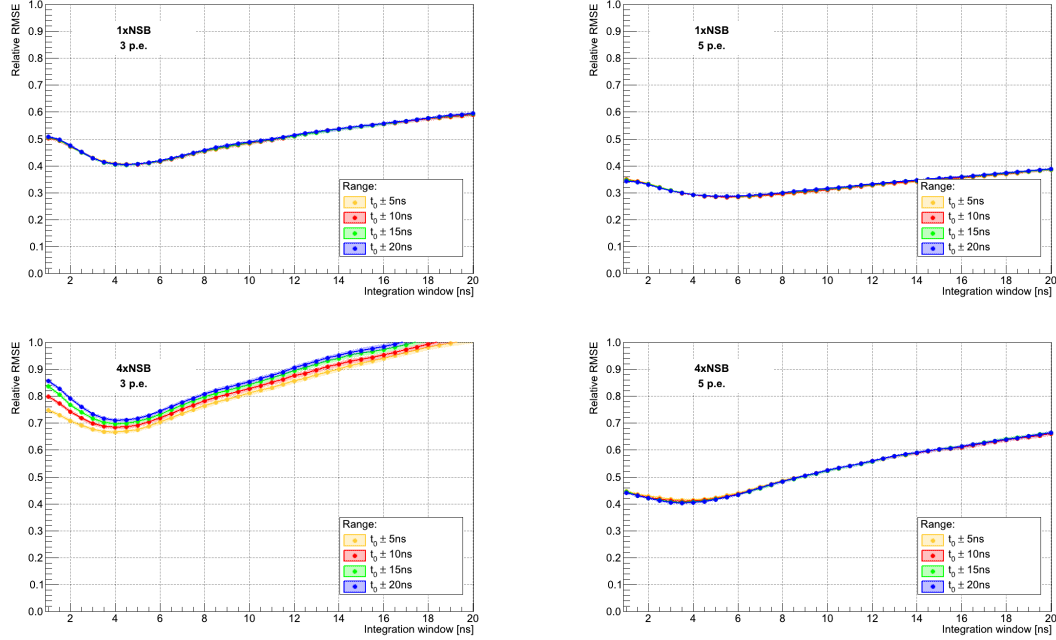


Figure A.9.: Relative RMSE for the broadening window algorithm `ChargeBroadeningSpline`, analogous to Figure A.7.

List of Abbreviations

CTA Cherenkov Telescope Array

CV coefficient of variation

FACT First G-APD Cherenkov Telescope

FoV Field of View

GRB gamma-ray burst

IACT Imaging Air Cherenkov Telescope

LST Large-Size Telescope

MAGIC Major Atmospheric Gamma-Ray Imaging Cherenkov Telescopes

MST Medium-Size Telescope

NSB night sky background

PDE photon detection efficiency

PMT photomultiplier tube

QE quantum efficiency

RMSE root mean square error

SST Small-Size Telescope

List of Figures

2.1.	Astroparticle physics at a schematic glance.	3
3.1.	Schematic sketch of an extensive air shower induced by a gamma-ray and by a cosmic ray hadron.	7
3.2.	Shower images simulated with the program CORSIKA.	8
3.3.	Picture of the MAGIC telescopes.	9
3.4.	Draft of the Cherenkov Telescope Array.	10
3.5.	Draft of the three telescope types and possible configurations of the telescopes for the northern and the southern site.	11
3.6.	Picture of the FACT telescope.	12
3.7.	Schematic of a photomultiplier tube.	13
3.8.	Picture of a SiPM.	14
3.9.	G-APD pulse waveforms on an oscilloscope according to the number of measured photons.	14
4.1.	Example of a simulated readout sample and the mean of 1000 readout samples.	17
4.2.	Results of the signal charge obtained with different integration windows.	19
4.3.	Example of a linear interpolation.	21
4.4.	Example of a spline interpolation.	21
4.5.	Two examples for a fixed integration window.	22
4.6.	Example of an unpreferred result of a sliding window.	23
4.7.	Comparison of the different arrival time definitions.	24
4.8.	Flow chart to illustrate the implemented classes, their callable functions and their inheritances.	27
5.1.	Example of calibration factors.	32
5.2.	Relative RMSE for different ratios related to the arrival time.	34
5.3.	Relative RMSE for the integration method Sum.	35
5.4.	Relative RMSE for the integration methods Interpolation and Spline.	36
5.5.	Relative RMSE for the window method Fixed.	37
5.6.	Relative RMSE for the window methods Sliding and Broadening.	38
5.7.	Relative RMSE to compare different telescope sizes.	39
5.8.	Relative RMSE to compare different NSB rates.	40
5.9.	Relative RMSE to compare different sampling rates.	41
5.10.	Mean of the extracted arrival time.	43
5.11.	RMS of the extracted arrival time.	44

6.1.	Example of a simulated readout sample.	46
6.2.	Comparison between a simulated and a real readout sample.	46
6.3.	Influence of range and integration window on the calibration factor.	47
6.4.	Relative RMSE to adjust the ratio.	48
6.5.	Relative RMSE for an algorithm analogous to the one used in PARFACT. . .	49
6.6.	Relative RMSE for the algorithm <i>SlidingSum</i>	49
6.7.	Relative RMSE of the chosen algorithms in direct comparison.	50
6.8.	Relative RMSE as a function of number of photoelectrons.	51
6.9.	Relative RMSE as a function of number of photoelectrons.	52
A.1.	Relative bias for a fixed window algorithm.	56
A.2.	Relative bias for a sliding window algorithm.	57
A.3.	Relative bias for a broadening window algorithm.	57
A.4.	Relative RMS for a fixed window algorithm.	58
A.5.	Relative RMS for a sliding window algorithm.	59
A.6.	Relative RMS for a broadening window algorithm.	59
A.7.	Relative RMSE for a fixed window algorithm.	60
A.8.	Relative RMSE for a sliding window algorithm.	61
A.9.	Relative RMSE for a broadening window algorithm.	61

List of Tables

4.1. Mean and RMS of the distributions.	18
---	----

Bibliography

- [1] The CTA Consortium. Design concepts for the Cherenkov Telescope Array CTA: an advanced facility for ground-based high-energy gamma-ray astronomy. *Experimental Astronomy*, 32(3):193–316, 2011.
- [2] W. Wagner. *Design and Realisation of a new AMANDA Data Acquisition System with Transient Waveform Recorders*. PhD thesis, Universität Dortmund, 2004.
- [3] R. Stockli, A. Nelson, and F. Hasler. Big Blue Marble Earth. NASA, GSFC, NOAA, USGS, 2003. <http://apod.nasa.gov/apod/ap030426.html>.
- [4] J. Hester and A. Loll. M1: The Crab Nebula from Hubble. NASA, ESA, 2011. <http://apod.nasa.gov/apod/ap111225.html>.
- [5] C. Engelbracht et al. Smoke from the Cigar Galaxy. JPL, Caltech, NASA, 2006. <http://apod.nasa.gov/apod/ap060414.html>.
- [6] G. Fishman et al. BATSE GRB Final Sky Map. BATSE, CGRO, NASA, 2000. <http://apod.nasa.gov/apod/ap000628.html>.
- [7] Z. Levay. SN 1006 Supernova Remnant. NASA, ESA, 2009. <http://apod.nasa.gov/apod/ap090801.html>.
- [8] V. Beckmann et al. Molecular Torus Surrounds Black Hole. NASA's GSFC, ESA, 2004. <http://apod.nasa.gov/apod/ap040908.html>.
- [9] J.A. Hinton and W. Hofmann. Teraelectronvolt Astronomy. *Annual Review of Astronomy and Astrophysics*, 47(1):523–565, 2009.
- [10] B. Falkenburg and W. Rhode. *From Ultra Rays to Astroparticles - A Historical Introduction to Astroparticle Physics*. 2012.
- [11] C. Grupen. *Astroteilchenphysik - Das Universum im Licht der kosmischen Strahlung*. 2000.
- [12] J. Albert et al. for the MAGIC Collaboration. VHE Gamma-Ray Observation of the Crab Nebula and its Pulsar with the MAGIC Telescope. *The Astrophysical Journal*, 674(2):1037, 2008.
- [13] B. W. Carroll and D. A. Ostlie. *An Introduction to Modern Astrophysics*. Addison-Wesley, 2007.

- [14] J. Buckley et al. The status and future of ground-based TeV gamma-ray astronomy. 2008.
- [15] M. Amenomori et al. for the Tibet AS γ Collaboration. Observations of TeV Gamma Rays with the Tibet Air Shower Array and Future Prospects. *21st European Cosmic Ray Symposium*, 2008.
- [16] R. Atkins et al. for the Milagro Collaboration. Status of the Milagro Gamma Ray Observatory. *27sth International Cosmic Ray Conference*, 2001.
- [17] P. F. Michelson et al. Fermi gamma-ray Space Telescope: high-energy results from the first year. *Reports on Progress in Physics*, 73(7), 2010.
- [18] P. K. F. Grieder. *Extensive Air Showers: High Energy Phenomena and Astrophysical Aspects - A Tutorial, Reference Manual and Data Book, Vol. 1*. 2011.
- [19] M. V. S. Rao and B. V. Sreekantan. *Extensive Air Showers*. 1998.
- [20] F. Schmidt. CORSIKA Shower Images. <http://www.ast.leeds.ac.uk/~fs/showerimages.html>.
- [21] P. A. Čerenkov. Visible radiation produced by electrons moving in a medium with velocities exceeding that of light. *Phys. Rev.*, 52:378–379, 1937.
- [22] M. Backes. TU Dortmund, 2009.
- [23] J. Cortina for the MAGIC Collaboration. Highlights of the MAGIC Telescopes. *32nd International Cosmic Ray Conference*, 2011. <http://arxiv.org/abs/1110.4747>.
- [24] D. Borla Tridon et al. for the MAGIC Collaboration. Performance of the Camera of the MAGIC II Telescope. *31st International Cosmic Ray Conference*, 2009.
- [25] P. Antoranz Canales. *Contributions to the high frequency electronics of MAGIC II Gamma Ray Telescope*. PhD thesis, Universidad Complutense de Madrid, 2009.
- [26] D. Bastieri et al. for the MAGIC Collaboration. Observation of GRBs by the MAGIC Telescope, Status and Outlook. *30th International Cosmic Ray Conference*, pages 1127–1130, 2007.
- [27] G. Pérez Díaz. Instituto de Astrofísica de Canarias (Servicio Multimedia), 2012.
- [28] J. M. Davies and E. S. Cotton. Design of the quartermaster solar furnace. *The Journal of Solar Energy, Science and Engineering*, 1:16–22, 1957.
- [29] R. A. Cameron for the CTA Collaboration. Development of a mid-sized Schwarzschild-Couder telescope for the Cherenkov Telescope Array. *SPIE Astronomical Telescope and Instrumentation Conference*, 2012.
- [30] F. Temme. TU Dortmund, 2012.

- [31] CERN COURIER. Innovative camera records cosmic rays during full moon. 2011.
- [32] M. Backes et al. FACT - the First Cherenkov Telescope using a G-APD Camera for TeV Gamma-ray Astronomy. 2010.
- [33] Q. Weitzel et al. A novel camera type for very high energy gamma-ray astronomy based on geiger-mode avalanche photodiodes. *JINST* 4 P10010, 2009.
- [34] M. Backes et al. Long-term monitoring of blazars - the DWARF network. *31st International Cosmic Ray Conference*, 2009.
- [35] Hamamatsu Photonics K.K. *Photomultiplier Tubes - Basics and Applications*, 2006.
- [36] T. Krähenbühl et al. Geiger-mode Avalanche Photodiodes as Photodetectors in Cherenkov Astronomy. *31st International Cosmic Ray Conference*, 2009.
- [37] T. Krähenbühl et al. Results of the prototype camera for fact. *Nuclear Instruments and Methods in Physics Research Section A: Accelerators, Spectrometers, Detectors and Associated Equipment*, 639(1):55–57, 2011.
- [38] Hamamatsu Photonics K.K. Data sheet: Mppc - s10362-33 series, 2009.
- [39] D. Renker and E. Lorenz. Advances in solid state photon detectors. *Journal of Instrumentation*, 4, 2009.
- [40] A. M. Hillas. Cherenkov light images of eas produced by primary gamma. *19th International Cosmic Ray Conference*, 3:445–448, 1985.
- [41] R. K. Bock et. al. Methods for multidimensional event classification: a case study using images from a cherenkov gamma-ray telescope. *Nuclear Instruments and Methods in Physics Research Section A: Accelerators, Spectrometers, Detectors and Associated Equipment*, 516(2-3):511 – 528, 2004.
- [42] S. Lombardi et al. for the MAGIC Collaboration. Advanced stereoscopic gamma-ray shower analysis with the MAGIC telescopes. *32nd International Cosmic Ray Conference*, 2011.
- [43] J. Holder for the VERITAS Collaboration. VERITAS: Status and Performance. *Science with New Generation of High Energy Gamma-ray Experiments*, 2006.
- [44] Bartko et al. for the MAGIC Collaboration. Fadc signal reconstruction for the magic telescope. *Nuclear Instruments and Methods in Physics Research Section A: Accelerators, Spectrometers, Detectors and Associated Equipment*, 594(3):407 – 419, 2008.
- [45] Peter Cogan. *Nanosecond Sampling of Atmospheric Cherenkov Radiation Applied to TeV Gamma-Ray Observations of Blazars with VERITAS*. PhD thesis, University College Dublin, 2006.

- [46] R. Brun and F. Rademakers. ROOT - An object oriented data analysis framework. *Nuclear Instruments and Methods in Physics Research Section A: Accelerators, Spectrometers, Detectors and Associated Equipment*, 389(1-2):81–86, 1997.
- [47] H. Bartko et al. for the MAGIC Collaboration. Comparison of Signal Reconstruction Algorithms for the MAGIC Telescope. MAGIC internal TDAS note, 2005.
- [48] M.G. Kendall, A. Stuart, J.K. Ord, and A. O'Hagan. *Kendall's Advanced Theory of Statistics - Distribution Theory*, volume 1.
- [49] S. Vorobiov et al. Optimizing read-out of the NECTAr front-end electronics. *Nuclear Instruments and Methods in Physics Research Section A: Accelerators, Spectrometers, Detectors and Associated Equipment*, 695:394 – 397, 2012.
- [50] S. Vorobiov et al. NECTAr: New electronics for the Cherenkov Telescope Array. *Nuclear Instruments and Methods in Physics Research Section A: Accelerators, Spectrometers, Detectors and Associated Equipment*, 639:62 – 64, 2011.
- [51] K. Bernlöhr. Simulation of imaging atmospheric Cherenkov telescopes with CORSIKA and sim_telarray. *Astroparticle Physics*, 30(3):149 – 158, 2008.
- [52] J. Buss. FACT Camera Calibration - Measurement of the G-APD Gain and Development of a Pulse Template (preliminary). Diploma thesis (in preparation), TU Dortmund, 2013.
- [53] D. Neise. Private communication.
- [54] F. Temme. FACT - Data Analysis: Analysis of Crab Nebula Data using PARFACT a newly Developed Analysis Software for the First G-APD Cherenkov Telescope. Diploma thesis, TU Dortmund, 2012.

Acknowledgments

I would like to thank Prof. Dr. Wolfgang Rhode for the supervision of this master thesis and the possibility to work in a really interesting research field where I was able to gain many experiences. Furthermore I am very glad that he enabled me trips to interesting schools, conferences and a datataking shift on La Palma.

Many thanks to Prof. Dr. Claus Gößling for his time and effort as the second referee of this thesis.

I would also like to thank Prof. Dr. Jim Hinton (University of Leicester) for the idea for this topic in the context of the CTA project and Dr. Serguei Vorobiov (DESY Zeuthen) for providing me the CTA Monte Carlo simulations.

Additionally, I give thanks to Dipl. Phys. Dominik Neise and cand. Dipl. Phys. Jens Buss for their support within the FACT project and especially their support concerning the FACT Monte Carlo simulations.

I am happy that Dr. Michael Backes and Dipl. Phys. Marlene Doert have shared their knowledge with me and have helped me with fruitful discussions, an introduction and also a more in-depth examination into the research field of gamma-ray astronomy and statistics.

Furthermore, I am grateful to have been a member of the astroparticle physics group E5b in Dortmund. While providing me insights into other fields of work, they have motivated and inspired me. We have always cooperated well and supported each other in a positive working atmosphere and I do not want to miss such nice colleagues.

M. Sc. Tomasz Fuchs, B. Sc. Karsten Köster and M. Sc. Kai Schennetten have accompanied me during my physics study and have supported me mentally as well as spiritually.

Special thanks to M. Sc. Tomasz Fuchs, my family and friends for supporting me with love and appreciation, especially during the last five years. I know, it was not always easy with me. Thank you so much!

Eidesstattliche Versicherung

Ich versichere hiermit an Eides statt, dass ich die vorliegende Masterarbeit mit dem Titel "Signal Extraction Studies applied to CTA and FACT" selbstständig und ohne unzulässige fremde Hilfe erbracht habe. Ich habe keine anderen als die angegebenen Quellen und Hilfsmittel benutzt sowie wörtliche und sinngemäße Zitate kenntlich gemacht. Die Arbeit hat in gleicher oder ähnlicher Form noch keiner Prüfungsbehörde vorgelegen.

Ort, Datum

Unterschrift

Belehrung

Wer vorsätzlich gegen eine die Täuschung über Prüfungsleistungen betreffende Regelung einer Hochschulprüfungsordnung verstößt handelt ordnungswidrig. Die Ordnungswidrigkeit kann mit einer Geldbuße von bis zu 50.000,00 € geahndet werden. Zuständige Verwaltungsbehörde für die Verfolgung und Ahndung von Ordnungswidrigkeiten ist der Kanzler/die Kanzlerin der Technischen Universität Dortmund. Im Falle eines mehrfachen oder sonstigen schwerwiegenden Täuschungsversuches kann der Prüfling zudem exmatrikuliert werden (§ 63 Abs. 5 Hochschulgesetz - HG -).

Die Abgabe einer falschen Versicherung an Eides statt wird mit Freiheitsstrafe bis zu 3 Jahren oder mit Geldstrafe bestraft.

Die Technische Universität Dortmund wird ggf. elektronische Vergleichswerkzeuge (wie z.B. die Software "turnitin") zur Überprüfung von Ordnungswidrigkeiten in Prüfungsverfahren nutzen.

Die oben stehende Belehrung habe ich zur Kenntnis genommen.

Ort, Datum

Unterschrift